

# Spectroscopic Investigations of Intersystem Crossing and Triplet State Structure in Acetylene

by

Ryan L. Thom

Submitted to the Department of Chemistry  
in partial fulfillment of the requirements for the degree of

Doctor of Philosophy

at the

MASSACHUSETTS INSTITUTE OF TECHNOLOGY

May 2006  
[June 2006]

© Massachusetts Institute of Technology 2006. All rights reserved.

Author .....

Department of Chemistry

May 18, 2006

Certified by .....

Robert W. Field

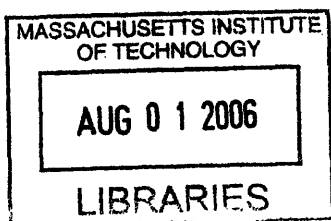
Haslam and Dewey Professor of Chemistry

Thesis Supervisor

Accepted by .....

Robert W. Field

Chairman, Department Committee on Graduate Students



ARCHIVED

This doctoral thesis has been examined by a Committee of the Department of Chemistry that included

Professor Sylvia T. Ceyer \_\_\_\_\_

(Chairman)

Professor Troy Van Voorhis \_\_\_\_\_

Professor Robert W. Field \_\_\_\_\_

(Thesis Supervisor)

# Spectroscopic Investigations of Intersystem Crossing and Triplet State Structure in Acetylene

by

Ryan L. Thom

Submitted to the Department of Chemistry  
on May 18, 2006, in partial fulfillment of the  
requirements for the degree of  
Doctor of Philosophy

## Abstract

A multispectral study employing both Ultraviolet Laser Induced Fluorescence (UV-LIF) and Surface Electron Ejection by Laser Excited Metastables (SEELEM) spectroscopies has yielded a complete characterization of singlet-triplet interactions relevant to intersystem crossing in the region of the  $3\nu_3$  vibrational level of the  $\tilde{A}^1A_u$  excited electronic state of acetylene. Intersystem crossing proceeds through a “doorway” state which has been plausibly assigned as a specific low-lying vibrational level of the third triplet electronic state,  $T_3$ . The predominantly  $T_{1,2}$  dark states observed in the SEELEM spectrum show the remarkable property of spectral regularity, in the sense that they are able to be arranged into smooth, well-behaved “vibrational levels” as judged from reduced rotational term value plots. This fact, together with the observation of essentially all the expected triplet density of states, strongly suggest that these triplet states fall into the “strongly coupled,” highly mixed regime.

Thesis Supervisor: Robert W. Field

Title: Haslam and Dewey Professor of Chemistry



# Acknowledgments

Any omissions in this accounting, not to mention infelicities of phrase, will, I hope, charitably be ascribed to exhaustion. In any event, a short thesis does not call for lengthy acknowledgements.

Firstly, I must thank Bob Field, whose insights and enthusiasm for science and ideas will always inspire me. His excitement, optimism, and patience pierced the darkness of many a low moment in my graduate research career.

At this time I remember the many members of the Field group past who accompanied me along this path: Kevin Cunningham, Leah Ruslen, and Michelle Silva. Selen Altunata and Dr. Manjula Canagartna acquainted me with the molecular beam apparatus they built. During his tenure as postdoc, Dr. Adya Mishra and I logged many hours of glorious combat with the SEELEM experiment, wondering where all the electrons had gone. In recent years Kyle Bittinger has provided invaluable experimental assistance (as well as good musical taste) in the lab. With Richard Duan I shared many enjoyable conversations on theological and other topics. Jason Clevenger became, and remains, a good and valued friend, and a beacon of hope from life beyond graduate school; Dan Byun remains so, as well, despite his translation to the Left Coast. To Adam Steeves, Bryan Wong, Jeff Kay, and Dr. Hans Bechtel, I wish the best in their future endeavors.

David Ward and I shared lodging for four years that could in no wise be called uninteresting, and our share of overseas adventures as well. I thank Serhan Altunata for his friendship, helpful criticism, and especially as a comrade in the final months, days and hours of thesis preparation, which would have been a much more unpleasant prospect without our frequent “smoke breaks” and, yes, beer drinking.

Finally, my most profound thanks are owed to my parents, my mother and my late father, for their encouragement and forbearance throughout this long process and indeed through my entire education; and to my brother. Now that my formal education is complete, I hope I will be able to commence the repayment of my vast debt to them.



# Contents

<b>1</b>	<b>Introduction</b>	<b>15</b>
1.1	Objectives . . . . .	15
1.2	The Low-Lying Electronic States of Acetylene . . . . .	16
1.3	Previous Experimental Studies of Triplet Acetylene . . . . .	17
1.4	Progress . . . . .	19
<b>2</b>	<b>Analysis of the Acetylene <math>S_1</math> <math>3\nu_3 \sim T_3</math> Spin-Orbit Perturbation</b>	<b>21</b>
2.1	Introduction . . . . .	21
2.2	Experimental details . . . . .	22
2.3	Results . . . . .	24
2.3.1	UV-LIF spectrum . . . . .	26
2.3.2	SEELEM spectrum . . . . .	38
2.3.3	Density of triplet states . . . . .	45
2.4	Conclusion . . . . .	50
<b>3</b>	<b>The Nature of the Acetylene <math>T_3</math> Doorway State</b>	<b>53</b>
3.1	Introduction . . . . .	53
3.2	Estimation of Vibrational Overlap Integrals: General Considerations .	56
3.3	Results for Acetylene . . . . .	59
3.4	Rotational Constant Considerations . . . . .	64
3.5	Assessing the Model and Conclusions . . . . .	68
3.6	Acknowledgements . . . . .	69

<b>4</b>	<b>Statistical Properties of SEELEM Spectra</b>	<b>71</b>
4.1	Introduction and Statement of Problem . . . . .	71
4.2	Random Matrix Theory and Statistical Properties of Spectra . . . . .	72
4.3	Numerical Simulations of Doorway-Mediated Coupling Cases . . . . .	75
4.4	Remarks and Conclusions . . . . .	77
<b>5</b>	<b>A High-Resolution SEELEM Spectrometer</b>	<b>83</b>
5.1	Motivation . . . . .	83
5.2	Design of the Single-Frequency Cw Laser Spectrometer . . . . .	85
5.3	Initial Results . . . . .	86
5.4	Future Prospects . . . . .	87
<b>6</b>	<b>Conclusion</b>	<b>89</b>



# List of Figures

1-1	Schematic cuts of low-lying acetylene potential energy surfaces along CCH bend coordinate; adapted from Ref. [50]. . . . .	17
2-1	Simultaneously recorded surface electron ejection by laser excited metastables (SEELEM, upper trace) and ultraviolet laser-induced fluorescence (UV-LIF, lower trace) spectra in the region of the $V_0^3K_0^1$ sub-band of the acetylene $\tilde{A}^1A_u \leftarrow \tilde{X}^1\Sigma_g^+$ electronic transition. Weak reproducible features in the wings have been magnified by a factor of 20. . . . .	25
2-2	Modified reduced term value plot displaying the rotational dependence of the $S_1 \sim T_3$ interaction, showing that the most important (i.e., resonant) interactions take place between $S_1$ and the $F_2$ spin component of $T_3$ . Crossing of the zeroth order energies of $S_1$ and $F_2$ takes place near $J = 3$ (difficult to see on this scale). . . . .	29
2-3	The reduced rotational term values of excited states observed in the UV-LIF spectrum plotted versus $N'(N' + 1)$ , with $\bar{B} = 1.127 \text{ cm}^{-1}$ (A) for $R$ -branch transitions, and (B) for $Q$ -branch transitions. Note that $R$ - and $Q$ -branch transitions belong to different $e/f$ symmetry components of the upper state. $P$ -branch transition energies are related to $R$ -branch transition energies by ground state combination differences. In addition, triplet state $S$ - and $O$ -branch transition energies are related to $Q$ -branch transition energies. Therefore, reduced term values derived from other branches ( $P$ , $S$ , and $O$ ) are not plotted. For $K = 0$ upper states, only $Q$ -branch transitions are possible. . . . .	39

2-4	Reduced rotational term values of triplet state vibrational levels identified in the SEELEM spectrum plotted vs. $N(N + 1)$ , with $\bar{B} = 1.127 \text{ cm}^{-1}$ , along with lines of best fit, for (A) $R$ -branch transitions and (B) $Q$ -branch transitions. Note that $R$ - and $Q$ -branch transitions terminate on different $e/f$ symmetry components of the upper state. $P$ -branch transition energies are related to $R$ -branch transition energies, and $S$ - and $O$ -branch transition energies are related to $Q$ -branch transition energies by ground state combination differences. Therefore, reduced term values derived from these branches are not plotted. . . .	45
2-5	Intensity vs. term value plot (Boltzmann plot) for the SEELEM spectrum. (A) $R$ -branch and (B) $Q$ -branch transitions. The numbers 1, 2, etc., correspond to the branches in Fig. 2-4, from top to bottom. Intensity is normalized by dividing by $S_J$ and $g_n$ , where $S_J$ is the rotational linestrength ( $J = N$ dependence factor in the intensity expression) and $g_n$ is the nuclear statistical weight factor. . . . .	51
3-1	Intersection seams between the $T_3$ and $T_2$ potential energy surfaces, calculated at the MR-CISD level, (a) as a function of the HCCH torsional angle and HCC bend angles under $C_2$ symmetry; (b) as a function of HCCH torsional angle and antisymmetric HCC bend, showing two seams of conical intersections. Figure taken from Ventura et al. [50]	55
4-1	A simulated rotational term plot, with $\langle B_{\text{dark}} \rangle = B_{\text{doorway}}$ and $\langle H_{\text{dark-dark}}^2 \rangle^{1/2} = 0.1 \text{ cm}^{-1}$ . . . . .	78
4-2	Same as previous, but with $\langle H_{\text{dark-dark}}^2 \rangle^{1/2} = 0.5 \text{ cm}^{-1}$ . . . . .	79
4-3	Same as previous, but with $\langle H_{\text{dark-dark}}^2 \rangle^{1/2} = 1 \text{ cm}^{-1}$ . . . . .	80
4-4	Same as previous, but with $\langle H_{\text{dark-dark}}^2 \rangle^{1/2} = 5 \text{ cm}^{-1}$ . . . . .	81

5-1 NO<sub>2</sub> laser induced fluorescence (LIF) excitation spectrum near 23,582 cm<sup>-1</sup>, showing Doppler-limited linewidth, demonstrating the capabilities of our high resolution visible cw laser. Spectrum was recorded with molecular beam of 1% NO<sub>2</sub> in He, at backing pressure of 625 Torr. 87



# List of Tables

2.1	Angular momentum dependence of matrix elements of $H_{so}$ in a Hund's case- $b$ basis, following the notation of Ref. [43]. Unprimed quantum numbers refer to the singlet state. . . . .	31
2.2	Observed line positions, intensities, and assignments of lines in the UV-LIF spectrum . . . . .	35
2.3	Molecular constants extracted from the UV-LIF spectrum . . . . .	38
2.4	Observed line positions ( $\text{cm}^{-1}$ ) and rotational assignments of transitions in the SEELEM spectrum . . . . .	42
2.5	$T_0$ and effective $B$ constants of triplet vibrational levels observed in the SEELEM spectrum . . . . .	46
3.1	$\tilde{A}$ State Normal Modes and Harmonic Frequencies, as calculated in Ref. [47] . . . . .	60
3.2	$\tilde{A}$ State Harmonic Force Constants, from fit of Ref. [47] . . . . .	60
3.3	Equilibrium Structures of the $\tilde{A}^1A_u$ State, as quoted in Ref. [47], and of the $T_3^3B$ State, as calculated in Ref. [50], and in this work . . . .	60
3.4	Calculated $T_3^3B$ State Normal Modes and Harmonic Frequencies . .	63
3.5	$\mathbf{T}$ Matrix for $T_3^3B$ state, as determined from <i>ab initio</i> calculation . .	64
3.6	Estimated Energies, and Vibrational Overlaps and Effective Spin-Orbit Matrix Elements with $S_1^3\nu_3$ , of the Lowest-Lying $T_3$ Vibrational Levels	64
3.7	$a$ -axis Coriolis coefficients for $T_3$ , calculated from <i>ab initio</i> normal-modes analysis . . . . .	68



# Chapter 1

## Introduction

### 1.1 Objectives

This thesis is a contribution to the understanding of singlet-triplet interaction and intersystem crossing in the acetylene molecule, as part of a larger effort to develop novel experimental techniques for the study of small gas-phase molecules in metastable electronically excited states. Such systems have posed great challenges to the molecular spectroscopist, not least because of the nominally spin-forbidden optical transitions by which the triplet state is accessed.

The primary experimental technique utilized in this project has been Surface Electron Ejection by Laser Excited Metastables (SEELEM). The principle of this detection scheme is the ejection of an electron that results from the deexcitation of a metastable electronically excited atom or molecule upon impact with a metal surface. If the *electronic* excitation energy exceeds the work function of the metal, an electron is ejected, and with amplification the resulting electron current can be used as a monitor of laser excitation of metastable states. The molecules traverse a flight zone 12-22 cm long before colliding with the metal surface; only those molecules that traverse this region with their electronic excitation intact can give rise to a SEELEM signal. This geometric constraint imposes a minimum lifetime on SEELEM-detectable states; depending on the precise positioning of the detector, this falls somewhere between 40 and 100  $\mu\text{s}$  for our apparatus. In principle, this detection scheme offers

several advantages over absorption- or fluorescence-based techniques: direct sensitivity to non-optically bright basis state characters; sensitive detection of weakly populated, very long-lived states; and time-of-flight (TOF) capability, useful for distinguishing intact metastable molecules from earlier-arriving metastable photofragments.

## 1.2 The Low-Lying Electronic States of Acetylene

Acetylene ( $C_2H_2$ ), in its ground electronic state ( $\tilde{X}^1\Sigma_g^+$ ), is linear in its equilibrium geometry and is described by the electronic configuration

$$(1\sigma_g)^2(1\sigma_u)^2(2\sigma_g)^2(2\sigma_u)^2(3\sigma_g)^2(1\pi_u)^4.$$

The first excited electronic states, and all of those relevant to the work described in this thesis, result from the orbital excitation  $\pi_u \rightarrow \pi_g^*$  and are stabilized by bending out of linearity. Indeed, the experimental observation [24], [25] of the *trans*-bent  $\tilde{A}^1A_u$  state is widely celebrated as the first demonstration of a polyatomic molecule undergoing a qualitative change in equilibrium geometry upon electronic excitation. Fig. 1-1 shows schematic views of the low-lying acetylene potential energy surfaces, sliced along the CCH bend coordinate. The first triplet potential surface ( $T_1$ ),  $^3\Sigma_u^+$  at linearity, possesses stable minima in both *trans*- and *cis*-bent geometries, which are denoted the  $\tilde{b}^3B_u$  and  $\tilde{a}^3B_2$  electronic states, respectively. The second and third surfaces ( $T_2$  and  $T_3$ ) are degenerate at linear geometries, giving rise to a  $^3\Delta_u$  electronic state.  $T_2$ , like  $T_1$ , supports both *trans*- and *cis*- bent minima, the  $\tilde{c}^3A_u$  and  $\tilde{d}^3A_2$  states, respectively. Despite its important role in singlet-triplet interaction in acetylene, little is certain about the equilibrium structure of the  $T_3$  surface, except that it is of lower symmetry than  $C_{2h}$  or  $C_{2v}$ .





$3\nu_3$  level is strongly mixed with a bath of triplet states, and that a specific rovibrational level of the  $T_3$  state is likely to play a key role in this coupling, noting that a surface crossing between  $S_1$  and  $T_3$  had been predicted to occur in the energy vicinity of  $\tilde{A}^1A_u 3\nu_3$  [28], [11], [10]. They also pointed out that  $T_3$  does not possess sufficient vibrational state density at the energy of  $\tilde{A}^1A_u 3\nu_3$  to account for the observed degree of fractionation, and so hypothesized that the role of  $T_3$  is to mediate the coupling of the  $\tilde{A}^1A_u 3\nu_3$  level to the bath of  $T_{1,2}$  states—the “*doorway*”-mediated coupling hypothesis.

- In 1994, Drabbels et al. [16] recorded a high (18 MHz) resolution spectrum of the  $V_0^3K_0^1$  and  $V_0^4K_0^1$  sub-bands. They observed a background dark state density on the order of  $10/\text{cm}^{-1}$ , which was consistent with the expected density of  $T_1$  states in this energy region. On the assumption of a direct singlet-triplet coupling model, these authors used the Lawrance-Knight deconvolution algorithm [27] to extract the zeroth-order energies of the dark states and their coupling strengths to the bright  $S_1$  state.
- Dupre, Green, and Field reported Zeeman Anticrossing (ZAC) experiments, exciting the  $v_3 = 0-3$  levels of the  $\tilde{A}^1A_u$  state. In a ZAC measurement, a single rovibrational level is excited and the resulting fluorescence monitored, while the strength of an external magnetic field is scanned (typically over a range of 0-8 T). States containing triplet electronic state character and therefore possessing a magnetic dipole moment are tuned in energy; when such a state is tuned into degeneracy with the fluorescing bright state, it mixes appreciable dark-state character into the bright state, resulting in a decrement to the fluorescence signal (due mainly to enhanced collisional quenching of the longer-lived eigenstate). The resulting anticrossing spectrum gives a panoramic view of the nearby triplet states capable of being Zeeman-tuned into resonance with the prepared singlet level. These acetylene ZAC spectra again showed a dramatic increase in the number of anticrossings with increasing excitation of the  $\tilde{A}^1A_u \nu_3$  mode.
- In 1998, Suzuki et al. [45] performed sensitized phosphorence measurements of

the lifetimes of metastable states accessible by intersystem crossing from the  $3\nu_3$   $K = 1$  and  $4\nu_3$   $K = 1$  levels of the  $\tilde{A}^1A_u$  state. The metastable molecules prepared by laser excitation in a jet were detected by sensitized phosphorescence upon impact with a biacetyl-coated surface. In these experiments, they measured the lifetimes of the metastable states as  $100 \mu\text{s}$  ( $3\nu_3$ ) and  $80 \mu\text{s}$  ( $4\nu_3$ ) respectively.

- In 1999, Ahmed, Peterka, and Suits [2] reported the first experimentally determined value for the electronic excitation energy of the lowest triplet state  $T_1$  ( $\tilde{a}^3B_2$ ) as  $28,900 \text{ cm}^{-1} = 82.65 \text{ kcal mol}^{-1}$ . They identified  $\tilde{a}^3B_2$  acetylene as a minor photodissociation (243 nm) product in their velocity map imaging study of the vinyl radical ( $\text{C}_2\text{H}_3$ ). This experimentally determined value, however, did not agree well with the recently reported *ab initio* value of  $30,500 \text{ cm}^{-1}$ .

## 1.4 Progress

It had been hoped that the second-generation SEELEM spectrometer, described in Ref. [3], would eventually be capable of recording large numbers of acetylene singlet-triplet transitions, providing valuable information about excitation energies, structures, and dynamics of triplet acetylene. Unfortunately, we were never able to maintain the apparatus at a consistently high level of performance, sufficient to attempt such experiments. Nevertheless, we are able to report some progress in our understanding of triplet states and intersystem crossing mechanisms in acetylene. In **Chapter 2**, we describe a refined analysis of the resonant singlet-triplet interaction in the important  $3\nu_3$  level of the  $\tilde{A}^1A_u \leftarrow \tilde{X}^1\Sigma_g^+$  electronic transition, made possible by an enhancement in experimental conditions (especially resolution). In particular, we were able to perform an unprecedentedly detailed analysis of the background triplet states illuminated by their doorway-mediated interaction with the  $S_1$   $3\nu_3$  bright state. One surprising result of this analysis was the discovery of an apparent regularization of the spectrum of these interacting dark states. This phenomenon is examined in greater detail in **Chapter 4**, with the aid of numerical simulations of the doorway-

coupled Hamiltonian model, in order to gain insight into what this observation reveals about the nature of the dynamics. In **Chapter 3**, the results of recent and original *ab initio* electronic structure calculations are used to make a tentative vibrational assignment of the  $T_3$  doorway state, an important step in formulating future experimental approaches to the characterization of the  $T_3$  state. **Chapter 5** describes progress in the construction of a high resolution laser system for use in SEELEM spectroscopy. Finally, **Chapter 6** summarizes our findings and discusses the future prospects of this project.

# Chapter 2

## Analysis of the Acetylene $S_1$

### $3\nu_3 \sim T_3$ Spin-Orbit Perturbation

#### 2.1 Introduction

The centrality of the  $3\nu_3$  (3 quanta in the symmetric CCH bend) vibrational level of the first excited singlet electronic state of acetylene ( $S_1 \tilde{A}^1A_u$ ) in intersystem crossing has long been recognized. The  $V_0^3K_0^1$  sub-band of the acetylene  $\tilde{A}^1A_u \leftarrow \tilde{X}^1\Sigma_g^+$  electronic transition is strongly perturbed by a great number of states, many of them magnetically sensitive or displaying other hallmarks of triplet character. One special triplet state, an unknown vibrational level of the sparse (at 45,300  $\text{cm}^{-1}$ ) manifold belonging to the third triplet electronic state  $T_3$ , has been hypothesized to play a special role as a “doorway” mediating singlet-triplet interaction. In a previous study [12], a single rotational series appearing in the  $P$ - and  $R$ -branches of the UV-LIF spectrum of this sub-band was identified as the  $T_3$  triplet perturber, and incorporated in a  $3 \times 3$   $J$ -dependent Hamiltonian fitting model, along with the main  $S_1 3\nu_3$  series and a Franck-Condon-dark  $S_1$  vibrational level observed through anharmonic interaction. Some additional LIF features were identified as predominantly triplet in character, but were neither rotationally assigned nor included in any fit. A subsequent study [3] demonstrated the doorway-mediated mechanism of the singlet-triplet interaction by means of statistical properties of the groupings of SEELEM lines about each LIF

feature. Yet these investigations have left some key *spectroscopic* questions unanswered. If the doorway state is a triplet, then how does its threefold spin multiplicity manifest itself in the UV-LIF/SEELEM spectrum? Can the doorway features be definitively assigned quantum numbers ( $N$ ,  $K$ ,  $J$ , vibrational assignment) that locate them in a manifold of  $T_3$  rovibrational states, of which hopefully an entire series will eventually be identified? Here we present a more detailed description and analysis of the spin-mixed molecular eigenstates observed in this spectrum, which allow some of these questions to be answered. The majority of the material in this chapter has been published as an article in the *Journal of Molecular Spectroscopy*.

## 2.2 Experimental details

The acetylene UV-LIF and SEELEM spectra are recorded in a two-chamber pulsed supersonic jet apparatus which has been described previously [3]. The source chamber houses a pulsed valve, which generates a pulsed supersonic molecular jet impinging on a skimmer at the entry to the detector chamber. The SEELEM detector [12] is located in the detection chamber, at a distance of 18 cm from the pulsed valve, 16.5 cm from the laser excitation region, and 15 cm from the skimmer. A base pressure of  $8 \times 10^{-8}$  torr was routinely achieved in the detector chamber with no molecular beam pulsing; typical operating pressures with the pulsed valve in operation were about  $3 \times 10^{-7}$  torr. This relatively lower operating pressure enhances the quantum efficiency of the SEELEM detector compared to what had been achieved in a previous apparatus, which typically operated at  $1 \times 10^{-5}$  torr [12]. A molecular beam of acetylene is formed by expansion of 1 atm of premixed acetylene (BOC Gases, purified by several freeze-pump-thaw cycles using liquid nitrogen) and helium in a 1:9 ratio, through a 0.5-mm diameter pulsed nozzle (R.M. Jordan), operated at 10 Hz, into the source chamber. The frequency-doubled output of a Lambda Physik FL 3002 dye laser, operated with Coumarin 440 dye and pumped by Nd:YAG third harmonic (355 nm) (Spectra Physics Model GCR-270 PRO, injection seeded, detection triggered off alternate pulses at 20 Hz and  $\sim 110$  mJ/pulse), intercepts the unskimmed molecular

jet 1.5 cm downstream from the pulsed valve and excites the acetylene molecules to the  $3\nu_3$  vibrational level of the  $\tilde{A}^1A_u$  state. About 1.5 cm downstream from the excitation region, the molecular beam passes through a 3-mm diameter electroformed skimmer (Precision Instruments) into the detector chamber and then travels  $\sim 15$  cm before colliding at normal incidence with the metal plate of the SEELEM detector. Because the SEELEM detector intercepts the skimmed molecular beam, the Doppler width of the SEELEM spectrum is reduced by a corresponding geometrical factor (metal plate diameter/total flight distance  $2.3 \text{ cm}/18 \text{ cm} = 0.1$ ), and thus the linewidth of the sub-Doppler SEELEM spectrum is laser-limited. From the SEELEM linewidths, the spectral full width at half maximum (FWHM) of the frequency-doubled laser is inferred to be  $0.05 \text{ cm}^{-1}$ ; the laser beam diameter is 3 mm, with an energy of 300-600  $\mu\text{J}/\text{pulse}$  ( $6 \times 10^3 \text{ kW}/\text{cm}^2$ ).

A photomultiplier tube (RCA Model 4501/V4, time response  $< 2.5 \text{ ns}$ , applied voltage 1 kV) directly views the excitation region of the unskimmed molecular beam in the source chamber and collects the UV-LIF signal through a pair of 1 in.-diameter biconvex quartz lenses located 3 cm above the molecular beam axis. The amplified UV-LIF signal is integrated by a gated integrator and boxcar averager (Stanford Systems, Model SR 250) and fed to a personal computer through a data-acquisition board (National Instruments, version 4.6, 1994 Edition). The UV-fluorescence collection electronics is gated on a delay of  $0.2 \mu\text{s}$  (to avoid scattered laser light), and off after 2-4  $\mu\text{s}$ . The SEELEM spectra are recorded simultaneously with the UV-LIF spectra. The SEELEM detector comprises a metal surface (gold in the present work, heated to  $300^\circ\text{C}$  to minimize the buildup of acetylene and fragmentation products on the metal surface) and an electron multiplier (ETP, SGE Instruments, Model AF831H,  $10^5$  gain). On impact with the gold surface, the metastable molecules are deexcited and an electron is ejected from the metal surface, provided that the vertical deexcitation energy is greater than the work function of the surface (for Au,  $\Phi = 5.1 \text{ eV}$ ). These ejected electrons are captured by the electron multiplier, sent through a fast preamplifier (EG&G Ortec 9301, gain 10) and an amplifier and discriminator unit (EG&G Ortec 9302, gain 20), and counted by a multichannel scaler

(Oxford Instruments). The SEELEM signal is summed over 60 laser pulses at each frequency increment (typically  $0.015\text{ cm}^{-1}$  in the doubled output) as the excitation laser is scanned. Frequency calibration ( $\pm 0.02\text{ cm}^{-1}$  accuracy) is accomplished by using the dye laser fundamental to record the absorption spectrum of  $^{130}\text{Te}_2$  [7] simultaneously with the LIF and SEELEM spectra. The SEELEM and UV-LIF spectra were smoothed and a multi-peak Gaussian fit (standard package in OriginLab Origin, version 6.1) was used to determine the positions and intensities (integrated peak area) of the spectral lines. The multi-peak Gaussian fit package was useful for determining the wavenumber and relative intensity of each of several partially overlapped lines.

## 2.3 Results

Figure 2-1 shows a portion of the simultaneously recorded SEELEM and UV-LIF spectra in the region of the  $V_0^3K_0^1$  sub-band of the acetylene  $\tilde{A}^1A_u \leftarrow \tilde{X}^1\Sigma_g^+$  electronic transition. The superficial similarity of the two spectra in their gross contours belies the fact that no one transition can appear in both the UV-LIF and the SEELEM spectrum. From the 300 ns lifetime of a pure  $S_1\ 3\nu_3$  basis state and the selected gate window of the PMT, we know that transitions appearing in the UV-LIF channel must terminate on eigenstates that have  $>1.4\%$  fractional  $S_1$  character (corresponding to  $\tau < 20\ \mu\text{s}$ ). These states comprise the Franck-Condon bright  $S_1$  vibrational state ( $3\nu_3, K = 1$ ), several Franck-Condon or  $K = 1$  dark  $S_1$  states (which derive their excitation intensity *via* anharmonic, Coriolis, or axis-switching interaction with the bright  $3\nu_3, K = 1$  state), and the  $T_3$  doorway state (which derives excitation and fluorescence intensity *via* spin-orbit interaction with the bright state). In contrast, the SEELEM spectrum consists of transitions terminating on eigenstates with  $<1.4\%$   $S_1$  bright state character ( $\tau > 20\ \mu\text{s}$ ), the dominant character of which is highly excited vibrational levels of the  $T_1$  and  $T_2$  electronic states, which gain their excitation intensity *via* spin-orbit interaction with the  $T_3$  doorway state.



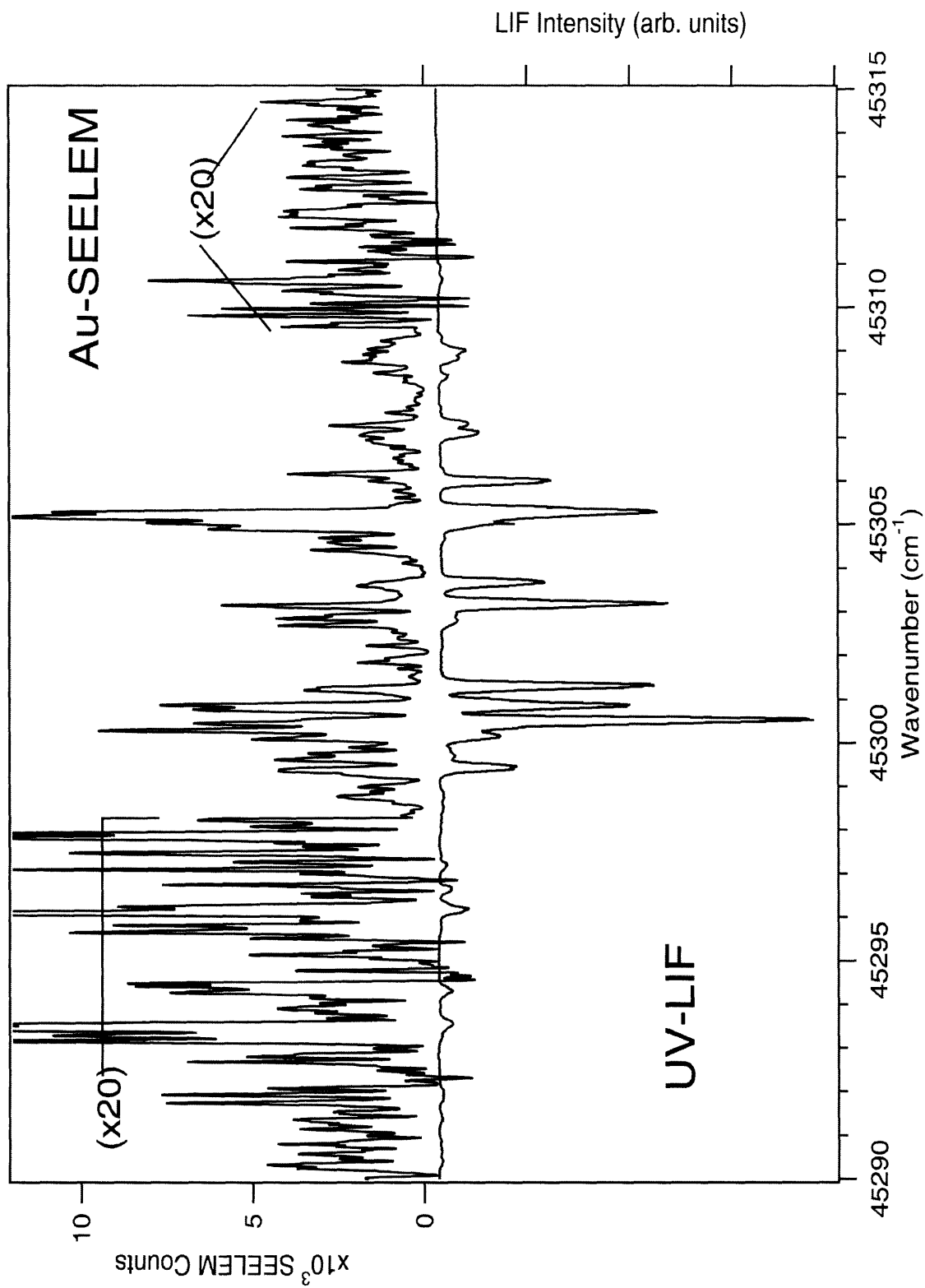


Figure 2-1: Simultaneously recorded surface electron ejection by laser excited metastables (SEELM, upper trace) and ultraviolet laser-induced fluorescence (UV-LIF, lower trace) spectra in the region of the  $V_0^3 K_0^1$  sub-band of the acetylene  $\tilde{A}^1 A_u \leftarrow \tilde{X}^1 \Sigma_g^+$  electronic transition. Weak reproducible features in the wings have been magnified by a factor of 20.

### 2.3.1 UV-LIF spectrum

#### Spectroscopy of the $T_3$ doorway state

The principal new result concerning the UV-LIF spectrum is the spin and rotational assignments of  $N' - J'' = 2, 1, 0, -1, -2$  ( $S, R, Q, P, O$ ),  $K' = 1$  rotational branches of one sub-band of the  $T_3 \leftarrow S_0$  electronic transition. These assignments provide information about the electronic symmetry, spin splitting, band origin, and  $B$  and  $C$  rotational constants of the doorway triplet state. The nominally forbidden triplet-singlet transition is made allowed by spin-orbit interaction of the excited triplet state with a nearby (near-resonant) singlet state. In the general case, such a transition is made allowed by admixture of bright character from potentially many, usually unknown, remote singlet states. For this situation, Hougen [22] has provided a detailed theoretical derivation of rotational selection rules and linestrength factors of triplet-singlet transitions in near-symmetric top molecules such as acetylene. The acetylene  $T_3$  electronic state has been predicted (see Chapter 3) to possess a minimum in  $C_2$  symmetry, within which its orbital symmetry species is  ${}^3B$ ; the totally symmetric ground state transforms as  ${}^1A$ . The rotational selection rules for such a transition are the least restrictive:  $\Delta N = 0, \pm 1, \pm 2$  and  $\Delta K = 0, \pm 1, \pm 2$ . Although Hougen's intensity expressions are useful for analyzing a transition into an isolated triplet level illuminated by spin-orbit interaction with remote singlet perturbers, a *resonant* interaction such as we find here between  $T_3$  and  $S_1$   $3\nu_3$  will result in energy shifts and intensity patterns that must be accounted for using an effective Hamiltonian perturbation model. A detailed discussion of spin-orbit selection rules and matrix elements needed for such a model follows below.

In the presence of resolvable spin-splitting (each triplet state rotational level with quantum number  $N$  splits into three spin components:  $J = N + 1$  ( $F_1$ ),  $J = N$  ( $F_2$ ),  $J = N - 1$  ( $F_3$ )), the triplet-singlet transition consists of two  $P$ - and two  $R$ -branches, three  $Q$ - branches and one  $O$ - and one  $S$ -branch. However, no resolvable triplet splitting was *directly* observed in the present work, except possibly two shoulders on  $Q$  transitions with a separation of  $\sim 0.14$   $\text{cm}^{-1}$ .  $R(0)$  and  $P(2)$  lines appear as

unresolved doublets. The  $J$  and  $N$  ( $J = N$ ) assignments of  $P$ - and  $R$ -branch lines are established based on the ground-state combination differences:

$$\tilde{\nu}[R(N) - P(N + 2)] = 2B''(2N + 3), \quad (2.1)$$

while, in the absence of resolved triplet spin splittings, two additional ground state combination differences,

$$\tilde{\nu}[S(N) - Q(N + 2)] = 2B''(2N + 3), \quad (2.2)$$

$$\tilde{\nu}[Q(N) - O(N + 2)] = 2B''(2N + 3), \quad (2.3)$$

are used to determine the rotational quantum numbers  $J$  and  $N$  in  $S$ -,  $Q$ - and  $O$ -branch lines ( $J = N - 1$  is reached *via* an  $S$ -branch line,  $J = N + 1$  *via* an  $O$ -branch line). Here it is important to mention that the right-hand sides of Eqs. 2.2 and 2.3 are identical and a particular lower-state combination difference may correspond to any one of the three possible branch pairs. For example, two lines separated by  $10B''$  can be assigned as either  $R(1)$  and  $P(3)$ , or  $S(1)$  and  $Q(3)$ , or  $Q(1)$  and  $O(3)$ . However, it is always possible to make a definite assignment by taking into account the relative intensities of the two lines. One of the three components of the  $Q$ -transition ( $F_3$ ) must exhibit an exact ground state combination difference with the unique  $S$ -branch transition ( $J' = J'' + 1$ ,  $N' = J'' + 2$ ), and another component ( $F_1$ ) must do the same with the unique  $O$ -branch transition ( $J' = J'' - 1$ ,  $N' = J'' - 2$ ). This information was used to assign the  $J'$  values of the  $Q$ -lines.

The analysis of a near-resonant singlet-triplet perturbation such as is seen here in the  $S_1 \sim T_3$  interaction can be facilitated by a modified reduced term value plot of the type displayed in Fig. 2-2. In principle, every  $S_1$  rotational level may interact with all three spin components ( $N = J, J \pm 1$ ) of the  $T_3$  rotational levels, so long as the selection rule  $\Delta J = 0$  is obeyed. Since this criterion for interaction is expressed in terms of  $J$ , the approximate Hund's case (*b*) triplet rotational energy expression

$$E_{rot} = T_0 + BN(N + 1) \quad (2.4)$$

is recast in terms of  $J$  for each of the three spin components as

$$E_{rot} = T_0 + \begin{cases} B(J+1)(J+2) \\ BJ(J+1) \\ BJ(J-1) \end{cases} \quad (2.5)$$

These term values are then reduced by subtracting some arbitrary rotational energy term  $\bar{B}J(J+1)$  to obtain

$$E_{red,T} = T_{0,T} + \begin{cases} (B - \bar{B})J^2 + (3B - \bar{B})J + 2B \\ (B - \bar{B})J(J+1) \\ (B - \bar{B})J^2 - (B + \bar{B})J \end{cases} \quad (2.6)$$

If  $\bar{B}$  has been chosen to equal very nearly  $B$ , then these expressions, when plotted against  $J$  (*not*  $J(J+1)$ ), will yield three straight lines, of, respectively: slope  $2B$  and intercept  $T_0 + 2B$ ; slope zero and intercept  $T_0$ ; and slope  $-2B$  and intercept  $T_0$ . The singlet rotational energies, when reduced by *the same* subtraction, remain, in general, quadratic in  $J$ :

$$E_{red,S} = T_{0,S} + (B_S - \bar{B})J(J+1) \quad (2.7)$$

and yield a parabola when plotted against  $J$ . Using such a scheme, the strongest (i.e., near-resonant) singlet-triplet interactions are clearly displayed as lying near singlet-triplet curve crossings. Such a plot was constructed, using molecular constants inferred from the spectrum, and is displayed in Fig. 2-2 (with  $45,300 \text{ cm}^{-1}$  as the origin of energy), for that asymmetry component of  $S_1$  observed in  $P$ - and  $R$ - branch lines ( $e$ -symmetry). This plot shows clearly that with this set of molecular constants, the dominant interaction experienced by the  $S_1$  rotational levels is that with  $F_2$  components of  $T_3$  levels of the same  $N$ , at least at the low- $J$  values sampled in the jet-cooled spectrum.

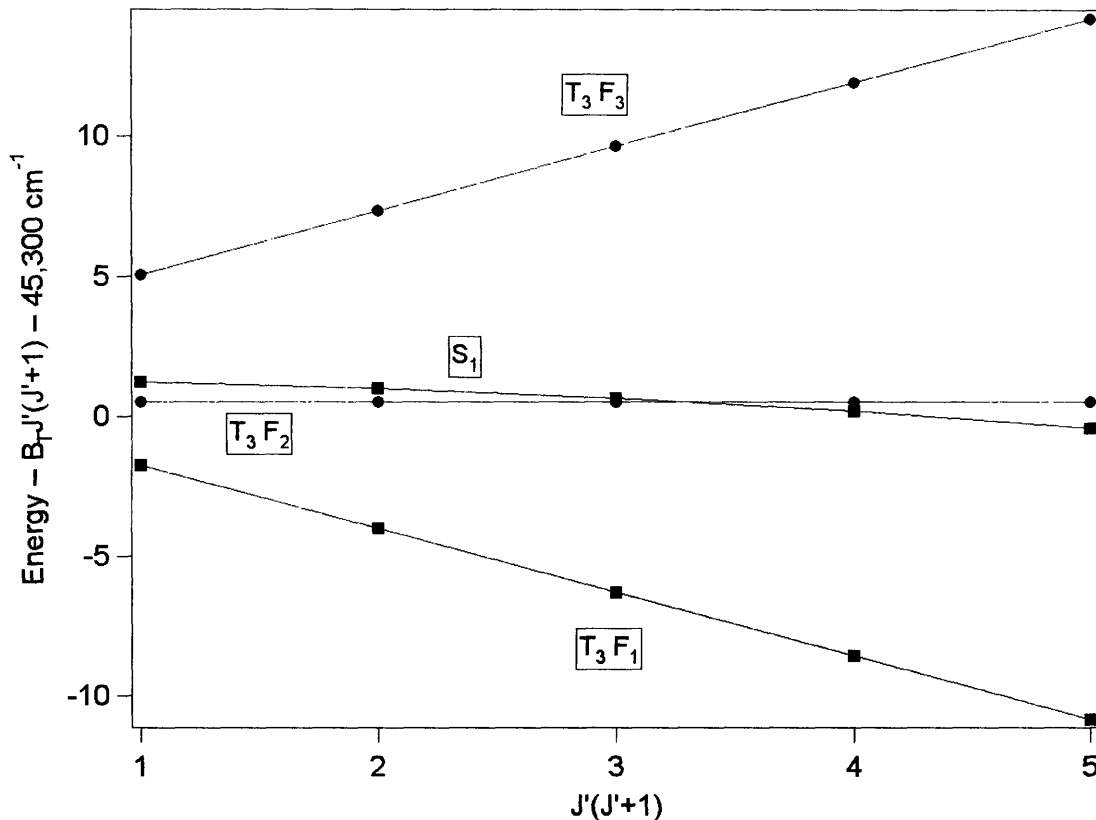


Figure 2-2: Modified reduced term value plot displaying the rotational dependence of the  $S_1 \sim T_3$  interaction, showing that the most important (i.e., resonant) interactions take place between  $S_1$  and the  $F_2$  spin component of  $T_3$ . Crossing of the zeroth order energies of  $S_1$  and  $F_2$  takes place near  $J = 3$  (difficult to see on this scale).

### Spin-Orbit Matrix Elements and Selection Rules

The number of analyzed resonant singlet-triplet interactions for polyatomic molecules in the literature is not large, and it is perhaps for this reason that the relevant interaction matrix elements and their quantum-number dependences are less well known than, for example, those pertaining to anharmonic resonances in IVR problems. Brand and Stevens [6] analyzed several triplet perturbations of vibrational levels of the  $^1A_2$  excited electronic state of formaldehyde, which they ascribed to second-order spin-rotation coupling (as opposed to direct spin-orbit interaction). Singlet-triplet perturbations have also been well characterized both experimentally and theoretically in the methylene radical  $CH_2$  [30], a species with spin-orbit interactions of about the

same magnitude as acetylene.

As an approximation to the full relativistic molecular Hamiltonian, various complicated “microscopic” spin Hamiltonians describing the interaction of electronic magnetic moments with the magnetic fields arising from electronic orbital and nuclear rotational motion, and the interaction of unpaired electronic magnetic moments with each other, have been given. The formulation of effective Hamiltonians for molecular spin interactions dates to the seminal paper of Van Vleck [49], which dwelt on analogies between molecular and atomic vector-coupling models. Raynes [39] used Van Vleck’s effective spin Hamiltonian to derive expressions for spin splittings in asymmetric rotors. Stevens and Brand [43] derived expressions for the angular momentum dependence of interaction matrix elements, both for direct spin-orbit coupling (which is operative in acetylene) and two second-order mechanisms (spin-orbit-orbital rotation and vibronic spin-orbit) which are important in orthorhombic species such as formaldehyde, for which the direct interaction is forbidden, but which do not concern us here.

The rotational energy level pattern of light molecules such as acetylene is generally well described by Hund’s case *b*, although the effect of spin-orbit is most naturally described in a case *a* basis, in which molecular rotation can be treated separately from the vibronic problem. In the nonrotating molecule, spin-orbit interaction splits each vibronic state into three components symbolized by  $|{}^{ev}\Gamma_T\Gamma_\sigma\rangle$ , where  $|{}^{ev}\Gamma_T\rangle$  represents the vibronic wavefunction of the triplet state (which solves the non-relativistic, purely vibrational Schrodinger equation), while  $|\Gamma_\sigma\rangle$  is the molecule-fixed spin function. These spin functions transform as rotations in the vibronic point group of the molecule, and are accordingly denoted  $\Gamma_\sigma(R_x)$ ,  $\Gamma_\sigma(R_y)$ , and  $\Gamma_\sigma(R_z)$ . The basis set for the rotating-molecule problem is generated by constructing products of these spin-vibronic basis functions with symmetric-rotor functions  $|JP\rangle$ , where  $J$  is the total angular momentum quantum number and  $P$  represents its signed projection along the molecular top  $z$ -axis. This basis set is closely related to the Hund’s case *a* basis  $|{}^{ev}\Gamma_TJSP\Sigma\rangle$ , the members of which are characterized by the molecule-fixed spin projection  $\Sigma$  as a good quantum number, rather than transformation as a representation

Table 2.1: Angular momentum dependence of matrix elements of  $H_{so}$  in a Hund's case- $b$  basis, following the notation of Ref. [43]. Unprimed quantum numbers refer to the singlet state.

$\Delta N$	$\Delta K$	$\langle {}^{ev}\Gamma_S N J K   H_{so}   {}^{ev}\Gamma_T N' J K' \rangle$
+1	0	$+[(J - K + 1)(J + K + 1)/(J + 1)(2J + 1)]^{1/2} \langle V_S   V_T \rangle \langle H_{so}(R_z) \rangle$
0	0	$+ \{K/[J(J + 1)]^{1/2}\} \langle V_S   V_T \rangle \langle H_{so}(R_z) \rangle$
-1	0	$-[(J^2 - K^2)/J(2J + 1)]^{1/2} \langle V_S   V_T \rangle \langle H_{so}(R_z) \rangle$
+1	$\pm 1$	$\mp [(J \pm K + 2)(J \pm K + 1)/4(J + 1)(2J + 1)]^{1/2} \langle V_S   V_T \rangle \{ \langle H_{so}(R_x) \rangle \mp i \langle H_{so}(R_y) \rangle \}$
0	$\pm 1$	$+ [(J \mp K)(J \pm K + 1)/4J(J + 1)]^{1/2} \langle V_S   V_T \rangle \{ \langle H_{so}(R_x) \rangle \mp i \langle H_{so}(R_y) \rangle \}$
-1	$\pm 1$	$\mp [(J \mp K - 1)(J \mp K)/4J(2J + 1)]^{1/2} \langle V_S   V_T \rangle \{ \langle H_{so}(R_x) \rangle \mp i \langle H_{so}(R_y) \rangle \}$
		$\langle H_{so}(R_\alpha) \rangle = \langle \Gamma_S   H_{so}(R_\alpha)   \Gamma_T \Gamma_\sigma(R_\alpha) \rangle$

of the vibronic point group:

$$| \Sigma = 0 \rangle = | \Gamma_\sigma(R_z) \rangle \quad (2.8)$$

$$| \Sigma = 1 \rangle = -2^{1/2} [ | \Gamma_\sigma(R_x) \rangle + i | \Gamma_\sigma(R_y) \rangle ] \quad (2.9)$$

$$| \Sigma = -1 \rangle = 2^{1/2} [ | \Gamma_\sigma(R_x) \rangle - i | \Gamma_\sigma(R_y) \rangle ]. \quad (2.10)$$

The phases of Eqs. 2.8-2.10 have been chosen to agree with the convention of Condon and Shortley [8]. Finally, the case- $b$  basis set  $| {}^{ev}\Gamma_T N J S k \rangle$  is obtained by the transformation

$$| {}^{ev}\Gamma_T N J S k \rangle = \sum_{P, \Sigma} \langle J S P \Sigma | J S N k \rangle | {}^{ev}\Gamma_T J S P \Sigma \rangle, \quad (2.11)$$

in which the coefficients  $\langle J S P \Sigma | J S N k \rangle$  differ slightly in phase from the standard Clebsch-Gordan coefficients given, e.g., by Condon and Shortley [8].

By carrying out these successive transformations, one can express spin-orbit matrix elements between case- $b$  states in terms of elements between the nonrotating-molecule spin components, along with a dependence on the rotational quantum numbers  $J$  and  $K$ . Table 2.1 collects the results for symmetric tops ( $K = |k|$ ). The selection rules for these matrix elements are seen to be  $\Delta N = 0, \pm 1$  and  $\Delta K = 0, \pm 1$ , where  $\Delta K = 0$  interactions occur between states of vibronic symmetries for which  ${}^{ev}\Gamma_S \otimes {}^{ev}\Gamma_T = \Gamma(R_z)$ , while  $\Delta K = \pm 1$  interactions occur when  ${}^{ev}\Gamma_S \otimes {}^{ev}\Gamma_T = \Gamma(R_x)$

or  $\Gamma(R_y)$ . In the case of asymmetric top molecules, the appropriate basis functions assume the form  $2^{-1/2}(|+K\rangle \pm |-K\rangle)$  rather than  $|\pm K\rangle$ . Matrix elements between these basis functions are identical to those in Table 2.1, except when  $\Delta K = \pm 1$  and  $K = 0$  for one of the states, in which case the corresponding matrix element must be multiplied by  $2^{1/2}$ .

The point group relevant to *trans*-bent acetylene is  $C_{2h}$ ; if as usual we label the *a*-inertial axis as the *z*-axis, and the twofold rotation axis as the *y*-axis, then  $\Gamma(R_y) = A_g$ , while  $\Gamma(R_x) = \Gamma(R_z) = B_g$ . Thus, for the interaction of  $S_1$  ( ${}^1A_u$ ) with  $T_3$  ( ${}^3B_u$ ), both  $\Delta K = 0$  and  $\Delta K = \pm 1$  couplings are possible ( $A_u \otimes B_u = B_g$ ). The situation is exactly the same if the symmetry is reduced to  $C_2$  ( $\Gamma(R_y) = A$ ;  $\Gamma(R_x) = \Gamma(R_z) = B$ ). Thus, *a priori*, the  $T_3$  state perturbing  $3\nu_3$  ( $K = 1$ ) could have  $K = 0, 1$ , or  $2$ . The observation of perturbations in both the *R*- and *Q*-branches (i.e., of both asymmetry components of  $3\nu_3$ ) precludes the assignment  $K = 0$ , while the observation of a triplet perturber with  $N = 1$  rules out the possibility of  $K = 2$ . Accordingly, we assign the  $T_3$  perturber as  $K = 1$ ; Table 2.1 provides all the spin-orbit matrix elements necessary for fitting this interaction using a model of spin-orbit-coupled asymmetric rotors.

### Singlet perturbors

All of the lines observed in the UV-LIF spectrum near the  $V_0^3 K_0^1$  sub-band of the  $\tilde{A} {}^1A_u \leftarrow \tilde{X} {}^1\Sigma_g^+$  electronic transition are listed in Table 2.3.1. Observed line intensities span a range of four orders of magnitude. Owing to effects which we describe below, the actual absorption line strengths probably span a range even wider than  $10^4$ . It was possible to establish rotational assignments for most of the lines. Table 2.3.1 includes all assignable rotational lines of the  $S_1 \leftarrow S_0$  transition and of its  $S_1$  and  $T_3$  perturbors. The  $J'$ -assignments of the *P*- and *R*-branch lines in singlet-singlet transitions are established by the well-known ground-state combination differences, as given by Eq. 2.1. For the assignments of *Q*-lines, a reduced term value plot, a Boltzmann intensity plot ( $\log I$  vs.  $N(N + 1)$ ), with intensities normalized with respect to nuclear statistical weights, and *a priori* known  $J$ -dependent factors such as



Hönl-London factors and axis-switching  $J$ -dependent intensity factors, were utilized. The singlet perturber earlier identified as  $\nu_2 + 2\nu_4$  by Scherer *et al.* [41] has been reassigned as one of the five members of the  $4\nu_b$  ( $b$  stands for “bend”) polyad by Utz *et al.* [48] The fundamental vibrational frequencies of  $\nu_4$  (torsion) and  $\nu_6$  (antisymmetric in-plane bend) in the  $\tilde{A}$  state are nearly identical, so overtone and combination levels involving  $\nu_4$  and  $\nu_6$  are profoundly mixed by Darling-Dennison 2:2 anharmonic resonances and by 1:1  $a$ -type Coriolis interactions. The  $4\nu_b$  polyad comprises the five basis states:  $(\nu_4, \nu_6) = (0, 4), (1, 3), (2, 2), (3, 1)$  and  $(4, 0)$ . Of these, only the three levels ( $4\nu_4, 2\nu_4 + 2\nu_6$ , and  $4\nu_6$ ) have the correct vibrational symmetry ( $A_g$ ) to perturb the  $3\nu_3$  level (and each other) by anharmonic interaction. The  $4\nu_b$  level that perturbs  $S_1 3\nu_3$  ( $K = 1$ ) *via* anharmonic resonance must have  $K = 1$ .

In the UV-LIF spectrum, four sub-bands are identified as consisting exclusively of  $Q$ -branch transitions. With known upper- and lower-state energies, one of these is assigned as the known  $V_0^3 K_0^0$  sub-band [51], which obtains its strength *via* the axis-switching mechanism [23]. The intensities of lines in the  $\Delta K = 0$  axis-switching sub-band increase with  $J$  as [23]  $J(J + 1)(2J + 1)$ , and lines with high  $J$  ( $> 6$ ) have been observed by Watson *et al.* [51] Our high signal-to-background ratio (enhanced by rotational cooling in the supersonic jet) allows us to observe the low- $J$  lines, freed of overlap with much stronger high- $J$  lines. Two members of the  $4\nu_b$  polyad, namely,  $4\nu_4$  (predicted vibronic energy,  $T_0 = 45,299$  and  $45,370$   $\text{cm}^{-1}$  for  $K = 0$  and  $1$ , respectively) and  $3\nu_4 + \nu_6$  ( $T_0 = 45,291$  and  $45,301$   $\text{cm}^{-1}$  for  $K = 0$  and  $1$ , respectively) are predicted by Merer [32] to line in the vicinity of  $S_1 3\nu_3 K = 1$  ( $T_0 = 45,301$   $\text{cm}^{-1}$ ). The anomalously large  $K = 0,1$  splitting in the nominal  $4\nu_4$  ( $A_g$  symmetry) level and the small  $K = 0,1$  splitting in the nominal  $3\nu_4 + \nu_6$  ( $B_g$  symmetry) level is due to  $a$ -type Coriolis interaction between  $K = 1$  levels. We have observed two sub-bands, in both cases exclusively  $Q$ -branch transitions, near the predicted locations of the  $K = 0$  components of these two vibrational levels. The vibrational symmetry of  $4\nu_4$  is  $A_g$ ; therefore, the  $K = 0$  levels of the  $4\nu_4$  state have  $f$ -symmetry for all  $J$  values. Therefore, only  $Q$ -branch transitions to the  $K = 0$  levels of the  $4\nu_4$  state from the  $e$ -symmetry ground-state rotational levels of  $S_0$  are allowed.

Thus, we assign the upper state of the  $Q$ -branch-only transition near  $45,298\text{ cm}^{-1}$  as  $4\nu_4$  ( $K = 0$ ), in agreement with Merer [32]. Merer also predicts a  $K = 0$  manifold of another  $S_1$  vibrational level near  $45,291\text{ cm}^{-1}$ ,  $3\nu_4 + \nu_6$ , where again we observe exclusively  $Q$ -transitions. However, this state *cannot* be assigned as  $3\nu_4 + \nu_6$  ( $K = 0$ ) because the vibrational symmetry of  $3\nu_4 + \nu_6$  is  $B_g$  and all rotational levels of this state with  $K = 0$  must have  $e$ -symmetry. Transitions to such a state would consist exclusively of  $P$ - and  $R$ - branch lines. An alternative assignment of the upper-state  $Q$ -transitions near  $45,291\text{ cm}^{-1}$  is  $4\nu_6$  with  $K = 0$ , which has the correct vibrational symmetry ( $A_g$ ) with  $f$ -symmetry for all  $J$  levels. Two sub-bands in the UV-LIF spectrum remain to be assigned, one with all three ( $P$ -,  $Q$ -,  $R$ -) branch types, and one with  $Q$ -transitions only. The upper states of these two sub-bands can be assigned to the only remaining vibrational level of  $A_g$  symmetry in the  $4\nu_b$  polyad, namely,  $2\nu_4 + 2\nu_6$ . The transitions terminating on the  $K = 1$  level of  $2\nu_4 + 2\nu_6$ , which are observed due to anharmonic interaction with  $3\nu_3$ , can have  $R$ -,  $Q$ -, and  $P$ -branches, whereas those terminating on the  $K = 0$  ( $f$ -symmetry) level can have only  $Q$ -branch transitions, as observed. The latter transition is due to axis switching.

The observed intensities of  $Q$ -branch transitions terminating on the  $4\nu_4$  ( $K = 0$ ) and  $4\nu_6$  ( $K = 0$ ) states merit comment. One possible cause for the observation of these transitions is Coriolis interaction between  $4\nu_4$   $K = 0$  (or  $4\nu_6$   $K = 0$ ) and the  $3\nu_3$  level induced by  $c$ -axis rotation [13]. However, the intensity of these  $K = 0$  sub-bands is comparable to that of the  $3\nu_3$   $K = 0$  axis-switching sub-band. This intensity is much too large to be due to a  $\Delta v = 7$  combined anharmonic plus  $c$ -axis Coriolis interaction between  $3\nu_3$   $K = 1$  and  $4\nu_4$   $K = 0$  (or  $4\nu_6$   $K = 0$ ). We believe that the intensity of the  $4\nu_4$   $K = 0$  and  $4\nu_6$   $K = 0$  sub-bands is due to axis switching, probably augmented by a fluorescence selectivity effect. Specifically, if these states relax to vibrational levels of the  $\tilde{X}^1\Sigma_g^+$  ground state *via* Franck-Condon-allowed transitions in a substantially different region of the spectrum from that to which  $3\nu_3$  radiates, nearer to the maximum response of the PMT, then the fluorescence detection is effectively biased in their favor, and against the  $3\nu_3$  states. Of course, a measurement of the *absorption* spectrum in this region would do much

to clarify these relative intensity observations. Finally, the transitions terminating on  $4\nu_6 K = 0$  are stronger than those terminating on  $4\nu_4 K = 0$  (see Table 2.3.1). This is in agreement with the finding of Mizoguchi et al. that the in-plane *trans*-bending  $\nu_3$  mode anharmonic interaction with the in-plane *cis*-bending  $\nu_6$  mode is stronger than that with the out-of-plane torsional  $\nu_4$  mode [29].

Table 2.2: Observed line positions, intensities, and assignments of lines in the UV-LIF spectrum

Transition		Wavenumber (cm <sup>-1</sup> )	Relative Intensity
$S_1 3\nu_3 \leftarrow S_0 (K_0^1)$	P(2)	45,296.166	110
	P(3)	45,293.545	77
	P(4)	45,290.643	12
	P(5)	45,287.855	5.0
	Q(1)	45,300.555	711
	Q(2)	45,300.158	256
	Q(3)	45,299.463	403
	Q(4)	45,298.506	20
	Q(5)	45,297.188	45
	R(0)	45,303.212	547
	R(1)	45,305.319	1000
	R(2)	45,307.127	175
	R(3)	45,309.047	119
	R(4)	45,310.695	23
	R(5)	45,312.192	15
$S_1 3\nu_3 \leftarrow S_0 (K_0^0)$	Q(1)	45,285.517	5.8
	Q(2)	45,285.106	3.5
	Q(3)	45,284.518	9.5
	Q(4)	45,283.618	0.2
	Q(5)	45,282.606	0.6
$S_1 (2\nu_4 + 2\nu_6) \leftarrow S_0 (K_0^1)$	P(2)	45,296.639	44

	P(3)	45,294.286	53
	Q(1)	45,298.262	6.4
	P(4)	45,291.994	12
	Q(1),Q(2),Q(3)	45,301.335	771
	R(0)	45,303.715	267
	R(1)	45,306.032	348
	Q(1)	45,291.818	13
	R(2)	45,308.443	28
$S_1 (2\nu_4 + 2\nu_6) \leftarrow S_0 (K_0^0)$	Q(1)	45,284.794	7.6
	Q(2)	45,283.923	5.6
	Q(3)	45,283.015	12
$T_3 \leftarrow S_0 (K_0^1)$	O(3)	45,288.613	30
	O(4)	45,283.366	0.6
	O(5)	45,277.699	4.4
	P(2)	45,295.740	14
	P(3)	45,293.296	17
	P(4)	45,290.876	7.8
	P(5)	45,287.645	3.0
	Q(1)	45,300.885	630
	Q(1)	45,300.439	488
	Q(2)	45,299.829	80
	Q(2)	45,299.685	35
	Q(3)	45,298.867	12
	Q(3)	45,298.725	17
	R(0)	45,302.845	75
	R(1)	45,305.061	264
	R(2)	45,307.353	115
	R(3)	45,308.846	83
	R(4)	45,310.958	11
	S(1)	45,310.487	6.4

$S_1 4\nu_4 \leftarrow S_0 (K_0^0)$	Q(1)	45,298.262	6.4
	Q(2)	45,297.999	3.5
	Q(3)	45,297.444	7.7
	Q(4)	45,296.332	8.3
$S_1 4\nu_6 \leftarrow S_0 (K_0^0)$	Q(1)	45,291.818	13
	Q(2)	45,291.404	16
	Q(3)	45,290.401	14
	Q(4)	45,289.403	7.0

### Molecular constants

The reduced term value plots constructed from the rotational and vibrational assignments of the UV-LIF spectrum, are shown in Fig. 2-3. It is clearly seen that the  $T_3$  state lies below the  $S_1 3\nu_3 K = 1$  in the absence of rotation, and that the rotational levels of the two states cross near  $J' = N' = 3$ . The reduced term values  $E_{red}(N)$  are obtained by subtracting the approximate rotational energy,  $\bar{B}N'(N' + 1)$  (where  $\bar{B} = 1.127 \text{ cm}^{-1}$ ), from the upper state energy  $T$  ( $=T_0 + (B - \bar{B})N'(N' + 1)$ ). That is,

$$E_{red}(N') = T_0 + (B - \bar{B})N'(N' + 1), \quad (2.12)$$

where  $T_0$  is the (rotationless) vibronic energy. When plotted against  $N'(N' + 1)$ , the reduced term values lie on nearly straight lines with slopes of  $(B - \bar{B})$  and intercepts of  $T_0$ . Rotational constants and rotationless vibronic energies obtained from the reduced term value plots for all observed levels of  $S_1$ ,  $T_3$ , and  $T_{1,2}$  are given in Table 2.3. Note that the two asymmetry components of a  $K = 1$  level have slightly different effective  $B$  values, and that the sense of this difference has diagnostic significance for the vibronic symmetry. Also listed in Table 2.3 are the molecular constants obtained from a fit to an effective Hamiltonian represented by a  $3 \times 3$  matrix, in which the bright state,  $S_1 3\nu_3$ , the singlet perturber  $4\nu_b$ , and the  $T_3$  doorway state form the basis. These are the three states that give rise to the pattern of dominant UV-LIF intensities. We did not include in the fit the other singlet perturbors (observed in the

Table 2.3: Molecular constants extracted from the UV-LIF spectrum

Parameter	Value	
	Estimate from reduced term value plot	From Hamiltonian fit
$T_0 (T_3, K = 1)$	45,300.666(148), 45,300.863(51)	45,300.523
$T_0 (S_1 3\nu_3, K = 1)$	45,300.988(36), 45,300.922(170)	45,301.366
$T_0 (S_1 2\nu_4 + 2\nu_6, K = 1)$	45,301.339(40)	45,301.123
$T_0 (S_1 3\nu_3, K = 0)$	45,285.736(21)	
$T_0 (S_1 2\nu_4 + 2\nu_6, K = 0)$	45,285.083(142)	
$T_0 (S_1 4\nu_4, K = 0)$	45,298.590(138)	
$T_0 (S_1 4\nu_6, K = 0)$	45,292.133(84)	
$B (T_3, K = 1)$	1.126(9), 1.019(2)	1.137
$B (S_1 3\nu_3, K = 1)$	1.107(2), 1.056(3)	1.078
$B (S_1 2\nu_4 + 2\nu_6, K = 1)$	1.179(5)	1.185
$B (S_1 3\nu_3, K = 0)$	1.072(1)	
$B (S_1 2\nu_4 + 2\nu_6, K = 0)$	1.001(18)	
$B (S_1 4\nu_4, K = 0)$	1.069(11)	
$B (S_1 4\nu_6, K = 0)$	1.039(7)	
$H_{S_1 3\nu_3 \sim T_3}^{so}$		0.126
$H_{S_1 \sim 4\nu_h}^{anh}$		0.237

UV-LIF spectrum) or the triplet perturbors that appear in the SEELEM spectrum, because the number of adjustable parameters in such a fit would be comparable with the number of data points. In Table 2.3, the molecular constants obtained from the term value plot and those obtained from the Hamiltonian fit differ slightly because the former parameters are perturbed molecular constants, while the latter are partially “deperturbed.” Note also that since only one  $K$ -component of each state is involved, the  $K$ -dependent rotational energy term  $(A - B)K^2$  has been absorbed into  $T_0$ .

## 2.3.2 SEELEM spectrum

### Rotational Assignments

We turn now to discussion of the predominantly dark, triplet eigenstates. In all of our experiments, the SEELEM channel is exclusively sensitive to the  $S_1$  or  $T_3$  character of the eigenstates, since only the  $S_1$  and  $T_3$  basis-state vertical electronic excitation energies exceed the work function of gold ( $\Phi(\text{Au})=5.1$  eV). The SEELEM signal is detected on a gold surface  $\sim 16.5$  cm downstream from the laser excitation

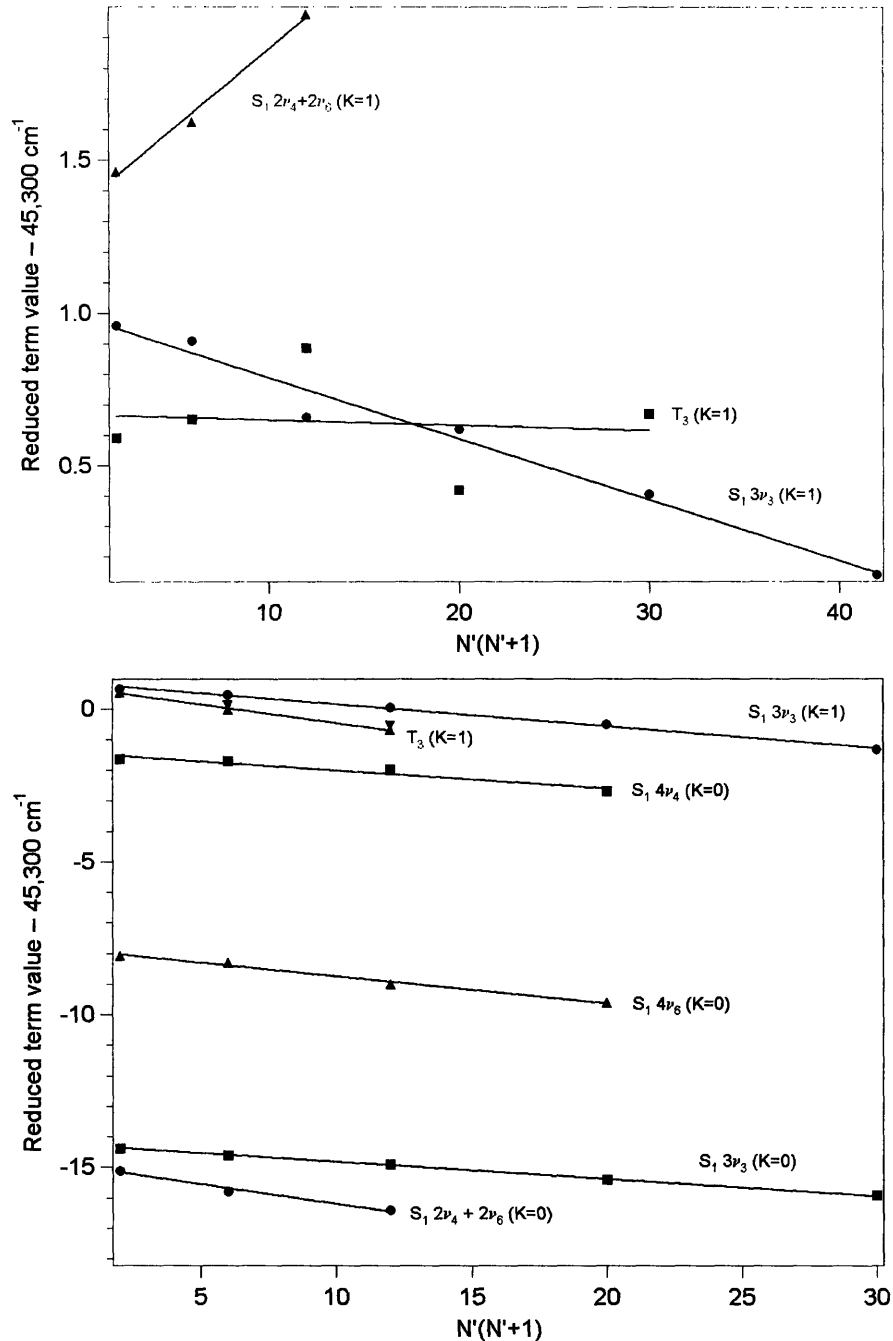


Figure 2-3: The reduced rotational term values of excited states observed in the UV-LIF spectrum plotted versus  $N'(N' + 1)$ , with  $\bar{B} = 1.127 \text{ cm}^{-1}$  (A) for  $R$ -branch transitions, and (B) for  $Q$ -branch transitions. Note that  $R$ - and  $Q$ -branch transitions belong to different  $e/f$  symmetry components of the upper state.  $P$ -branch transition energies are related to  $R$ -branch transition energies by ground state combination differences. In addition, triplet state  $S$ - and  $O$ -branch transition energies are related to  $Q$ -branch transition energies. Therefore, reduced term values derived from other branches ( $P$ ,  $S$ , and  $O$ ) are not plotted. For  $K = 0$  upper states, only  $Q$ -branch transitions are possible.

region; thus the SEELEM channel is exclusively sensitive to those eigenstates which remain electronically excited after the flight time (100-140  $\mu\text{s}$ ), yet which possess some  $S_1$  or  $T_3$  character. The SEELEM spectrum exclusively samples dark triplet states with radiative lifetimes greater than about 30  $\mu\text{s}$ . Note that Franck-Condon-dark  $S_1$  vibrational levels *cannot* appear in a SEELEM spectrum because, although the Franck-Condon factor (FCF) from  $\tilde{X}^1\Sigma_g^+$  is very small, these dark  $S_1$  vibrational levels radiate to high  $v''$  levels of  $S_0$  at a rate of  $1/(300 \text{ ns})$ . The radiative lifetime of a dark  $S_1$  level is not expected to be longer than that of a FC-bright  $S_1$  state (in fact, the lifetimes of these FC-dark levels might be shorter, since they experience weaker dilution of their oscillator strengths into triplet states) [15]. From the combination differences given by Eqs. 2.1-2.3, eight  $P$ -,  $R$ - branch pairs, five  $Q$ -,  $S$ - branch pairs, and five  $Q$ -,  $O$ -branch pairs could be identified in the SEELEM spectrum. Note that the strong  $\Delta N = \Delta J$  component of  $P$ - and  $R$ -branch transitions terminates on upper states with  $e$ -symmetry (in this study the ground state with  $l = 0$  contains exclusively  $e$ -symmetry rotational levels), while the strong  $\Delta N = \Delta J = \pm 1$  components of  $Q$ -,  $S$ -, and  $O$ - lines terminate on levels of  $f$ -symmetry. Since all of the rotational levels of a  $K = 0$  manifold must belong exclusively to either  $e$ - or  $f$ -symmetry, they are accessible from ground state rotational levels of  $e$ -symmetry either *via*  $P$ - and  $R$ -transitions ( $K' = 0$   $e$ -levels) or  $O$ -,  $S$ - and  $Q$ -transitions ( $K' = 0$   $f$ -levels). A manifold with  $K' \neq 0$  will be accessible *via* all five  $\Delta N = 0, \pm 1, \pm 2$  rotational branches. This explains why the observed number of  $R$ -,  $P$ -branch pairs can differ from the observed number of  $O$ -,  $Q$ - or  $Q$ -,  $S$ -branch pairs.

The observed positions ( $\text{cm}^{-1}$ ) and rotational assignments of lines in the SEELEM spectrum are listed in Table 2.4. Again, triplet spin splittings are not directly resolved. In this table we have not included those SEELEM lines (about 10 of 125) which did not fall onto a straight line on the reduced term value plots, although these “orphan” lines do satisfy a lower-state rotational combination difference for their respective values of  $N'$ . The rotational constants of dark triplet states and their  $N' = 0$  experimental vibronic energies,  $T_0$ , obtained from the reduced term value plot 2-4, are displayed in Table 2.5. The extracted  $B$  values of the dark states are



found to be very similar to that of the  $T_3$  doorway state. In Table 2.5, the  $K$  values of each observed triplet vibrational level and possible electronic symmetries are also listed. The sub-bands that terminate at a lowest observed  $N'$  value of 2 are assigned as  $K' = 2$ . The two effective  $B$  values corresponding to the  $e$ - and  $f$ -symmetry components of a  $K = 2$  manifold are observed to be nearly identical, which accords with the fact that asymmetry splittings of  $K = 2$  levels are generally much smaller than those of  $K = 1$ . The sub-bands with exclusively  $R$ -,  $P$ -branch pairs or  $Q$ -,  $S$ - and  $O$ -,  $Q$ -branch pairs belong, as mentioned above, to  $K' = 0$ . The remaining sub-bands that terminate at a lowest observed  $N'$  value of 1 are assigned as  $K' = 1$ , and the  $e$ -,  $f$ -symmetry components of these states are observed to possess significantly different effective  $B$  values. The electronic symmetry assignments of triplet states listed in Table 2.5 are based on the selection rules for singlet-triplet transitions and the symmetry requirements for  $\Delta K = 0$  and 1 singlet-triplet interaction *via*  $H^{so}$ . Since the  $A$  rotational constant of acetylene is on the order of 10-20  $\text{cm}^{-1}$  (and indeed for the computed  $T_3$  structure described in Chapter 3 is 24  $\text{cm}^{-1}$ ), only one of three possible  $K$  levels (0, 1, or 2) of a particular triplet vibrational level is expected to interact *resonantly* with the  $S_1$  or  $T_3$  doorway state, both of which have  $K = 1$ . Thus, it can be firmly concluded that observed triplet dark states with different  $K$  values belong to different vibrational levels.

Table 2.4: Observed line positions ( $\text{cm}^{-1}$ ) and rotational assignments of transitions in the SEELEM spectrum

$N$	$P(N+2)$	$R(N)$	$\Delta_1 = R(N) - P(N+1)$	$O(N+2)$	$Q(N)$	$S(N-2)$	$\Delta_2 = Q(N) - O(N+2)$	$\Delta_3 = S(N-2) - Q(N)$
0	45,296.510	45,303.578	7.068					
0	45,296.100	45,303.156	7.056					
0	45,295.817	45,302.856	7.039					
0	45,295.657	45,302.705	7.048					
0	45,295.351	45,302.409	7.058					
0	45,295.148	45,302.233	7.085					
1	45,294.413	45,306.164	11.751	45,289.006	45,300.780		11.774	
1	45,294.282	45,306.008	11.726	45,288.622				
1	45,294.140	45,305.770	11.630	45,288.535	45,300.305*		11.770	
1	45,293.545	45,305.305	11.760	45,287.625	45,299.387		11.762	
1	45,293.286	45,305.044	11.758					
1	45,293.156	45,304.917	11.761					
1	45,292.823	45,304.589	11.766					
1	45,292.675	45,304.411	11.736					
2	45,291.739	45,308.198	16.459	45,285.064	45,301.531	45,308.592	16.467	7.061

2	45,291.525	45,308.022	16.497	45,284.814	45,301.290	45,308.368	16.476	7.078
2	45,291.362	45,307.843	16.481	45,284.046	45,300.567	45,307.573	16.521	7.006
2	45,290.807	45,307.282	16.475	45,283.613	45,300.098	45,307.143	16.485	7.045
2	45,290.572	45,307.047	16.475	45,282.754	45,299.245	45,306.332	16.491	7.087
2	45,290.462	45,306.947	16.485					
2		45,306.612						
2	45,289.972	45,306.423	16.451					
3	45,288.923	45,310.096	21.172	45,279.957	45,301.215	45,312.974	21.258	11.759
3	45,288.794	45,309.959	21.165	45,279.646	45,300.888		21.242	
3	45,288.622	45,309.814	21.192	45,279.100	45,300.305*	45,312.076	21.205	11.771
3	45,288.039	45,309.230	21.191		45,299.765	45,311.492		11.727
3	45,287.854	45,309.042	21.188			45,311.378		
3	45,287.721	45,308.916	21.195		45,299.011	45,310.743		11.732
3	45,827.298	45,308.498	21.200					
3	45,287.195	45,308.364	21.169					
4		45,311.816			45,300.719			
4		45,311.614			45,300.463			
4	45,285.191	45,311.052	25.861		45,299.969			
4		45,310.860			45,299.354	45,315.835		16.479
4	45,284.502	45,310.395	25.893			45,315.383		

4	45,310.292		45,298.618	45,315.123	16.505
5			45,300.172		
5			45,299.906		
5			45,299.631		
5			45,298.772		
5			45,298.342		
6			45,298.103		

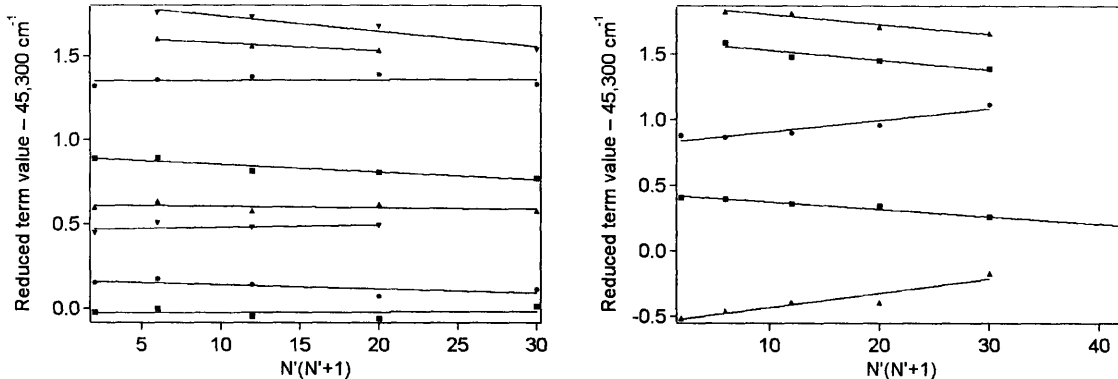


Figure 2-4: Reduced rotational term values of triplet state vibrational levels identified in the SEELEM spectrum plotted vs.  $N(N + 1)$ , with  $\bar{B} = 1.127 \text{ cm}^{-1}$ , along with lines of best fit, for (A)  $R$ -branch transitions and (B)  $Q$ -branch transitions. Note that  $R$ - and  $Q$ -branch transitions terminate on different  $e/f$  symmetry components of the upper state.  $P$ -branch transition energies are related to  $R$ -branch transition energies, and  $S$ - and  $O$ -branch transition energies are related to  $Q$ -branch transition energies by ground state combination differences. Therefore, reduced term values derived from these branches are not plotted.

### 2.3.3 Density of triplet states

One of the chief results of this work is the observation of nine spin-rotationally assigned vibrational levels of dark triplet states, spread over an energy range of  $2.42 \text{ cm}^{-1}$ , as can be gleaned from Table 2.5. This span of energy represents the widest spectral “window,” centered on the intensity-mediating  $T_3$  doorway features, through which the strength of the singlet-triplet interaction allows us to observe triplet spectral features of appreciable and reproducible intensity. This state count implies a vibrational density of dark triplet states of  $3.7/\text{cm}^{-1}$ . This density must, however, be reduced by a factor of 3 to account for the three possible  $K$ -values through which each triplet vibrational level can be sampled. By contrast, the density of (spin and rotationally unassigned) triplet states around  $S_1 3\nu_3$  extracted by Drabbels et al. from their deconvolution of their ultra-high resolution (18 MHz) LIF spectrum, is  $4.9/\text{cm}^{-1}$ . There are at least four possible reasons for this discrepancy: (i) some of the dark states belong, as we have shown, to  $S_1$  Franck-Condon dark states; (ii) at 18 MHz resolution, it could have been possible to resolve spin splittings, yet Drabbels et

Table 2.5:  $T_0$  and effective  $B$  constants of triplet vibrational levels observed in the SEELEM spectrum

$T_0$ (cm <sup>-1</sup> ) from		$B$ (cm <sup>-1</sup> ) from		Possible assignment
$R$ -branch trans. ( $e$ -symmetry)	$Q$ -branch trans. ( $f$ -symmetry))	$R$ -branch trans. ( $e$ -symmetry)	$Q$ -branch trans. ( $f$ -symmetry)	
45,301.828(30)	45,301.881(22)	1.118(2)	1.120(1)	$K = 2$
45,301.622(13)	45,301.606(34)	1.122(1)	1.120(3)	$K = 2$
45,301.353(25)	–	1.127(2)	–	${}^3B_u; K = 0$
45,300.901(17)	45,300.822(32)	1.123(1)	1.136(2)	${}^3B_u$ or ${}^3B_2; K = 1$
45,300.617(19)	–	1.126(1)	–	${}^3B_u; K = 0$
45,300.469(24)	45,300.428(11)	1.129(2)	1.122(1)	${}^3B_u$ or ${}^3B_2; K = 1$
45,300.170(25)	–	1.125(1)	–	${}^3B_u; K = 0$
45,299.974(26)	–	1.127(2)	–	${}^3B_u; K = 0$
–	45,299.461	–	1.138(2)	${}^3A_u; K = 0$

al. did not report any  $N$  assignments of coupled triplet states; (iii) some of the state density observed by these authors might have been due to fractionation into highly vibrationally excited levels of  $S_0$ , as had previously been observed in Zeeman anti-crossing (ZAC) and Zeeman quantum beat (ZQB) spectroscopy [18]; and (iv) we do not include in our state count rotationally assigned lines that could not be identified with a vibrational level by a smooth rotational term value plot. Our density of states, on the other hand, is based on direct observation of spin and rotationally assigned triplet states. It is possible that, with a resolution of only  $\sim 0.05$  cm<sup>-1</sup>, we were unable to resolve some rotational lines (particularly in the very congested  $Q$ -branch region) and failed to resolve or identify some of the coupled triplet states. With these facts in mind, one can say that the observed vibrational density of coupled triplet states (uncorrected for the contribution from three  $K$ -values) in the present work (3.7 states/cm<sup>-1</sup>) is in satisfactory agreement with that of [16] (4.9 states/cm<sup>-1</sup>).

Drabbels et al. [16] pointed out that the density of perturbing triplet states they observed could not be accounted for without invoking the participation of vibrational levels of the  $cis$ - $T_1$  ( ${}^3B_2$ ) potential minimum. In this connection, some comments seem warranted. First, since the  $S_1$   $3\nu_3$  energy region is now known to lie well above the barrier to  $cis$ - $trans$  isomerization on the  $T_1$  surface, the notion of vibrational levels belonging exclusively to either the  $cis$ - or the  $trans$ -minimum on the  $T_1$  surface

is misleading. Also, the calculated density of states given in Table 4 of [16], on which those authors based the above conclusion, appears to be incorrect. There are two errors in Table 4 of [16]: (i) the actual energy difference between the minima of the potential energy surfaces of the triplet states and the vibrational levels of  $S_1$  ( $3\nu_3$  and  $3\nu_4$ ) is larger for all triplet electronic states by  $\sim 3800 \text{ cm}^{-1}$  than the values specified in column 3 of Table 4, and (ii) the computed density of states presented in that table could only have been calculated with energies incorrectly measured from zero-point vibrational energies, rather than from potential minima. A corrected calculation shows that the total density of states of  $T_1$  at  $S_1$   $3\nu_3$  is  $5.6 \text{ states/cm}^{-1}$  ( $3.6$  for  ${}^3B_2$  *cis* plus  $2.0$  for  ${}^3B_u$  *trans*) and that for  $T_2$  is  $0.9 \text{ states/cm}^{-1}$  ( $0.2$  for  ${}^3A_2$  *cis* plus  $0.7$  for  ${}^3A_u$  *trans*).

Another fact not considered by Drabbels et al. [16] in the computed density of states is the vibrational symmetry of the triplet vibrational levels. Not all of the vibrational levels of the  $T_1$  and  $T_2$  surfaces can interact *via*  $H^{SO}$  with the  $S_1$   $3\nu_3$  state, due to vibrational symmetry selection rules. Only vibrational levels of the  $T_1$  and  $T_2$  states with  $A_g$  symmetry (out of four possible vibrational symmetries  $A_g$ ,  $B_g$ ,  $A_u$ , and  $B_u$ ) in *trans*-geometry or with  $A_1$  symmetry (out of  $A_1$ ,  $B_1$ ,  $A_2$ , and  $B_2$ ) in *cis*-geometry can directly mix with the  $S_1$   $3\nu_3$  state (in the absence of Coriolis perturbations). Thus the symmetry-sorted calculated total density of triplet states is  $(5.6 + 0.9)/4 = 1.6 \text{ states/cm}^{-1}$ , which is comparable to the value,  $\frac{3.7}{3} \text{ states/cm}^{-1}$ , observed in the present work and  $\frac{4.9}{3} \text{ states/cm}^{-1}$  reported (corrected for  $K$ ) in [16]. However, vibrational levels of  $B_g$  (or  $A_2$ ) symmetry of a triplet state can mix with the  $A_g$  (or  $A_1$ ) symmetry vibrational levels of the same  $K$  value through an *a*-type Coriolis interaction [13] (an order of magnitude weaker *c*- and *b*-type  $\Delta K = 1$  Coriolis interactions are also possible). As a result, two of the four vibrational symmetry species of  $T_1$  could in principle borrow bright character from the  $S_1$   $3\nu_3$  state or from  $T_3$ . This is exactly what has been observed in the SEELEM spectrum. The rotational levels of the upper and lower components of  $K$ -type doublets for  $K = 1$  should have *f*- and *e*-symmetries, respectively, if the  ${}^3B_u$  (or  ${}^3B_2$ ) has  $A_g$  (or  $A_1$ ) vibrational symmetry. Therefore, for  $K = 1$ , the effective  $B$  value obtained *via*

$Q$ -branch transitions ( $f$ -symmetry) should be greater than that for the  $R$ -branch ( $e$ -symmetry). In Table 2.5 this is true only for one observed  $K = 1$  level. The other  $K = 1$  vibrational level identified in Table must have  $B_g$  (or  $A_2$ ) vibrational symmetry, for which the labeling of  $e$ - and  $f$ -symmetries will be opposite to that for  $A_g$  (or  $A_1$ ) vibrational symmetry levels.

In the presence of “complete”  $a$ -type Coriolis mixing,  $\frac{1}{2}$  (rather than  $\frac{1}{4}$ ) of the vibrational levels of triplet states are capable of borrowing bright character. Therefore, the calculated density of coupled triplet vibrational states is  $(5.6 + 0.9)/2 = 3.3$  states/cm<sup>-1</sup>, which is only slightly larger than the observed density of coupled triplet states ( $\frac{3.7}{3}$  states/cm<sup>-1</sup>). Most of the triplet states identified in Table 2.5 have  ${}^3B_u$  or  ${}^3B_2$  symmetry and therefore belong to the  $T_1$  state. This is as expected, because the  $T_1$  state lies  $\sim 5500$  cm<sup>-1</sup> below the  $T_2$  state and its total vibrational density of states is 5.6 states/cm<sup>-1</sup>, compared to 0.9 states/cm<sup>-1</sup> for the  $T_2$  state at the energy of  $S_1 3\nu_3$ .

The regularity of the spectrum with respect to both the rotational energy level structure and the spectral intensities is a remarkable and surprising result. Anharmonic and  $a$ -type Coriolis mixing within the  $T_1$  state appear (from the observed density of vibrational states) to be essentially “complete” at these (high) vibrational energies. In a statistical sense, all vibrational levels of  $T_1$  are observed in the SEELEM spectrum, yet despite the completeness of the mixing, the rotational term curves (Fig. 2-4) are very regular and successive rotational levels unambiguously group themselves into unique, smooth, vibrational levels. Also, the intensities of SEELEM lines in a branch fall onto surprisingly smooth Boltzmann plots, as shown in Fig. 2-5. (Note that in Fig. 2-5, the intensity is normalized with respect to rotational linestrength,  $S_J$  ( $J$ -dependent factor from Table 3) and the nuclear statistical weight factor,  $g_n$ .) The large 3:1 intensity alternation is, therefore, no longer evident in the intensity plots after the line intensities have been corrected for the experimental  $S_J$  and  $g_n$ .) This regularity in the midst of the doorway-mediated interaction could be accounted for by one or both of two effects. First, the SEELEM spectra could exemplify a unique case of “strong” doorway state-dark state interaction. In the limit that the



average coupling matrix element,  $H_{\text{doorway-dark}}$ , between the doorway state and the nearby dark states, is large relative to  $\frac{1}{\rho_{\text{dark}}}$ , the average dark state level spacing, the spectrum exhibits a line-density approximately a factor of  $(\frac{\rho_{\text{dark}}}{\rho_{\text{doorway}}})$  times the line density in an unfractionated doorway state spectrum. Consecutive rotational levels of all dark states appear in the spectrum; thus the possibility exists that ground state combination differences could identify rotational levels that fall on smooth upper-state rotational term value plots that, in turn, would permit arrangement of dark state rotational levels into individual vibrational levels. The density of lines would make this a difficult, but in principle feasible, task. In the limit that  $H_{\text{doorway-dark}}$  is smaller than  $\frac{1}{\rho_{\text{dark}}}$ , then each rotational level of a doorway state fractionates into a small number of dark states. The energy window centered on each doorway state will have a width  $\sim \pm 3\langle H_{\text{doorway-dark}} \rangle$  because the second-order perturbation theoretic intensity of a transition at  $\Delta E = 3H_{\text{doorway-dark}}$  will be  $(\frac{H_{\text{doorway-dark}}}{\Delta E})^2 \approx \frac{1}{9}$  that of the transition into the doorway state.

However, even in this “weak” coupling limit, the possibility exists that the dark state rotational constants cluster with small dispersion around that of the doorway state. If  $B_{\text{doorway}} \approx \langle B_{\text{dark}} \rangle$ , then the doorway state window of width  $\sim 6H_{\text{doorway-dark}}$  moves in synchrony with consecutive rotational levels of the same set of dark states. Ground state rotational combination differences permit the dark states that remain systematically close to the doorway state for many rotational levels to be arranged into vibrational levels, giving again the same kind of spectral regularity observed here. Note that another weak coupling limit case is possible, for which  $B_{\text{doorway}} \neq \langle B_{\text{dark}} \rangle$ . Each doorway state rotational level illuminates a different set of dark state vibrational levels. This is the situation observed by Abramson et al. [1]. Clumps of resolved rotational lines were observed in stimulated emission pumping (SEP) spectra originating from successive rotational levels of acetylene  $\tilde{A}^1A_u$ . The intensity-weighted average energy of the clumps followed a smooth  $E(J)$  vs.  $BJ(J+1)$  plot, but the individual lines in successive  $J''$  clumps could not be arranged, *via* smooth rotational term value plots, into vibrational levels. In that case the typical Franck-Condon bright state apparently has a  $B$ -value quite different from  $\langle B \rangle$  of the Franck-

Condon dark states.

## 2.4 Conclusion

We have described here the most thorough analysis yet performed on the simultaneously recorded UV-LIF and SEELEM spectra in the region of the  $V_0^3K_0^1$  sub-band of the acetylene  $\tilde{A}^1A_u \leftarrow \tilde{X}^1\Sigma_g^+$  electronic transition. Intersystem crossing from an  $S_1$  bright state ( $3\nu_3$ ) to the dark triplet states is mediated by a single low-lying vibrational level of the  $T_3$  electronic state. We have characterized (spin-rotational analysis,  $J$ ,  $K$ , and  $N$  assignments, rotational constants) the bright state, the doorway state, and the dark states illuminated by the doorway state. New Franck-Condon dark singlet perturbers of the  $S_1$   $3\nu_3$  levels were identified ( $K = 0$  components of all three  $A_g$  symmetry members of the  $4\nu_6$  polyad and  $K = 1$  of  $2\nu_4 + 2\nu_6$ ). These states will be of interest in studying anharmonic and Coriolis interactions within the  $\tilde{A}^1A_u$  state, and possibly as intermediate states in double-resonance schemes interrogating highly vibrationally excited levels of the  $\tilde{X}^1\Sigma_g^+$  state. Our observations establish the doorway state as  $K = 1$ , and are consistent with a  $T_3$  electronic symmetry of  $^3B$ . From the SEELEM spectrum, we identify nine triplet vibrational levels, spread over  $\sim 2.42$   $\text{cm}^{-1}$ . It was possible to make unique  $K$ ,  $N$ , and  $J$ -value assignments for all of the triplet levels. Electronic symmetries are determined for seven of the nine triplet states. Most of the observed triplet dark states are assignable as  $T_1$  ( $^3B_u/{}^3B_2$ ;  ${}^3\Sigma_u^+$  in linear geometry), in agreement with the expected higher density of  $T_1$  versus  $T_2$  states. The observed density of triplet states implies that the  $A_g$  (or  $A_1$ ) and  $B_g$  (or  $A_2$ ) triplet vibrational levels are strongly mixed by nearly complete anharmonic and  $a$ -type Coriolis interactions and coupled to the bright state through the doorway state. Higher resolution spectra are desirable in order to enable a more definitive rotational analysis of these very densely spaced lines.

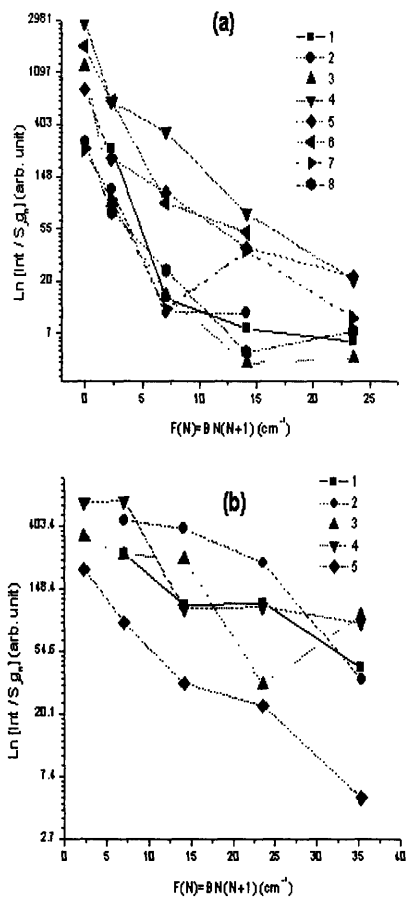


Figure 2-5: Intensity vs. term value plot (Boltzmann plot) for the SEELEM spectrum. (A) *R*-branch and (B) *Q*-branch transitions. The numbers 1, 2, etc., correspond to the branches in Fig. 2-4, from top to bottom. Intensity is normalized by dividing by  $S_J$  and  $g_n$ , where  $S_J$  is the rotational linestrength ( $J = N$  dependence factor in the intensity expression) and  $g_n$  is the nuclear statistical weight factor.



# Chapter 3

## The Nature of the Acetylene $T_3$ Doorway State

### 3.1 Introduction

We have described the detection, by surface electron ejection by laser-excited metastables (SEELEM) spectroscopy, of long-lived acetylene molecular eigenstates that must contain partial triplet basis-state character. What is clear from all of these SEELEM datasets is that the zeroth-order  $3\nu_3$  singlet state is perturbed by large numbers of zeroth-order triplet states; what is not immediately clear is whether these zeroth-order states can be assigned to one or more of the low-lying triplet potential energy surfaces. It is fairly well established that  $3\nu_3$  enjoys an unusually large coupling with triplets due to its proximity to a special “doorway” triplet level that mediates this coupling effectively. Previous studies [12], [3] have focused on the third triplet electronic state ( $T_3$ ) as the most likely candidate for providing this dynamical “doorway,” both by virtue of its relatively low density of vibrational levels in this energy region, and from consideration of the manner of its interaction with both  $S_1$  and lower lying triplets. The  $T_2$  and  $T_3$  electronic states are degenerate at linear nuclear geometries, where they represent the components of a  ${}^3\Delta_u$  state. *Ab initio* electronic structure calculations were slow in arriving at a consensus regarding the location and nature of the minimum of the  $T_3$  potential energy surface. Owing to the complexity and

computational expense of the problem, all geometry optimizations to date have been performed within symmetrical restrictions of configuration space—i.e., with geometries constrained to at least  $C_2$  (nonplanar, but with equal C-H bond lengths) or  $C_s$  (unequal C-H bond lengths, but planar) point group symmetries. Cui and Morokuma[10] were only able to locate a transition state (saddle point), with one imaginary normal-mode frequency along an antisymmetric CCH bending coordinate. More recently, Ventura et al.[50] performed extended multireference electron correlation calculations on all four of the lowest-lying acetylene triplet electronic states. These authors were able to find a genuine minimum (no imaginary frequencies) belonging to the  $T_3$  surface, whose properties are described below. The difficulties stem from the intricate manner in which the  $T_3$  and  $T_2$  surfaces interact. These two potential energy surfaces represent the two sheets of a Renner-Teller pair, being tangent at linear configurations, but this is not their only seam of intersection. Specifically, Ventura et al. describe two such seams lying very close to the predicted  $T_3$  stationary point. It is thus difficult to speak, in this energy region, of “pure”  $T_3$  or  $T_2$  vibronic levels, since they will be appreciably mixed with each other through non-adiabatic interactions. Indeed, these are among the interactions which make  $T_3$  such an effective doorway state in the first place. Thus, caution seems in order when proposing any vibrational “assignment” of the doorway state.

Nevertheless, a naive approach considering harmonic vibrational levels of pure  $T_3$  character may still provide a useful zeroth-order picture of the situation, and serve to leverage experimental observations. A previous partial deperturbation [12] extracted an effective  $S_1\ 3\nu_3\ T_3$  spin-orbit matrix element of  $\sim 0.1\ \text{cm}^{-1}$ ; our Hamiltonian fit (see Chapter 2) resulted in a similar value of  $0.126\ \text{cm}^{-1}$ . This represents the product of an electronic matrix element and a vibrational overlap integral. Cui, Morokuma, and Stanton [11] computed the purely electronic  $S_1 \sim T_3$  spin-orbit matrix element (i.e.,  $\langle S = 0, M_S = 0 | H^{SO} | S = 1, M_S = 1 \rangle$ ) as  $\sim 13.7\ \text{cm}^{-1}$ , at the minimum of the seam of intersection (MSX) of  $S_1$  and  $T_3$  in  $C_2$  symmetry. Thus, we require a vibrational overlap on the order of 0.01. *Ab initio* equilibrium geometries and force fields can be used to make semi-quantitative estimates of vibrational overlaps between  $S_1\ 3\nu_3$

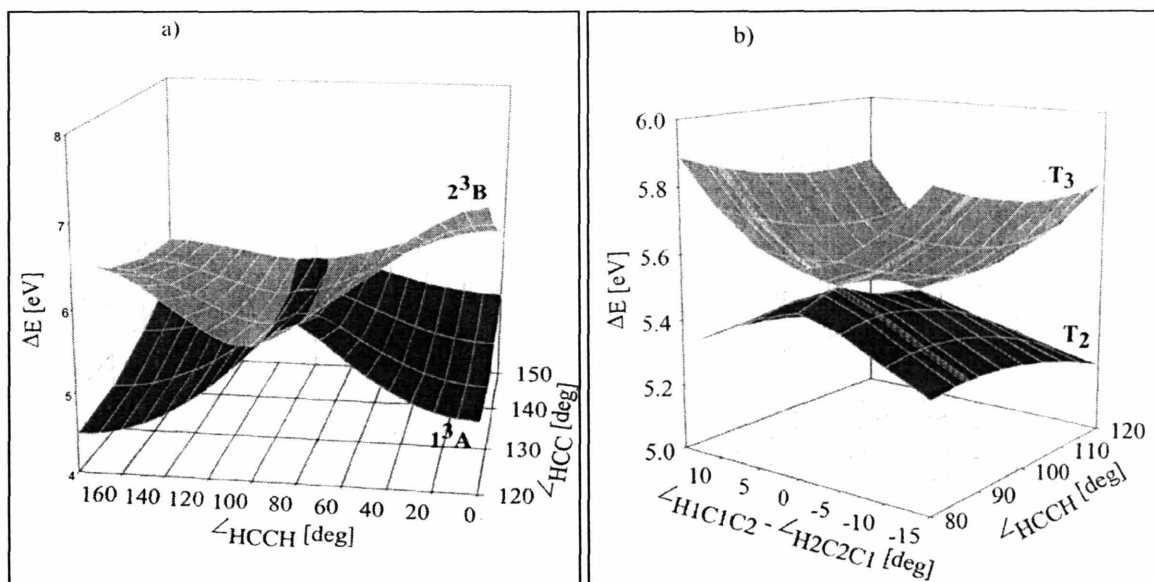


Figure 3-1: Intersection seams between the  $T_3$  and  $T_2$  potential energy surfaces, calculated at the MR-CISD level, (a) as a function of the HCCH torsional angle and HCC bend angles under  $C_2$  symmetry; (b) as a function of HCCH torsional angle and antisymmetric HCC bend, showing two seams of conical intersections. Figure taken from Ventura et al. [50]

and various low-lying  $T_3$  vibrational levels within the harmonic approximation. If something, at least, is known about the geometry and harmonic frequencies associated with the  $T_3$  minimum, then the overlaps of the lowest few vibrational levels of  $T_3$  with  $S_1 3\nu_3$  can be estimated. It would be satisfying if a  $T_3$  vibrational level predicted to lie near the energy of the  $3\nu_3$  level could be shown to possess an overlap in accord with the experimentally determined value. At the very least, the qualitative trends displayed by the results of such a calculation would not depend too sensitively on the precise values of the input parameters for the  $T_3$  equilibrium geometry and force constant matrix, and the expected strong dependence of overlaps on normal mode quantum numbers would be useful in ruling out vibrational candidates for the  $T_3$  doorway level.

## 3.2 Estimation of Vibrational Overlap Integrals: General Considerations

Multi-dimensional harmonic overlap calculations can be developed straightforwardly from the properties of harmonic-oscillator wavefunctions, expressed as functions of the nuclear normal coordinates. The principal complication in the polyatomic case arises from the necessity of expressing the wavefunctions of the two states in terms of a single integration variable, whereas in general the normal coordinates pertaining to two electronic states are referred to distinct equilibrium structures with different normal-mode vibrational frequencies, and thus the normal modes of one state are linear combinations of those of the other. The transformation connecting the two sets of normal coordinates consists of both displacements and the so-called Duschinsky rotation, which expresses the mixing of the respective normal coordinates. A compact matrix formulation of the problem is contained in the classic paper by Sharp and Rosenstock [42]. The fundamental starting point of the formalism is the “L-matrix” of normal-mode theory, which relates the normal mode coordinates ( $\mathbf{Q}$ ) to a complete set of internal displacement coordinates ( $\mathbf{S}$ ), i.e., bond lengths, bond angles, and torsional angles measured with respect to the equilibrium reference configuration:

$$\mathbf{S} = \mathbf{L}\mathbf{Q}. \quad (3.1)$$

If we explicitly write  $\mathbf{S}_i$  for a given equilibrium structure  $i$  as  $\mathbf{R} - \mathbf{R}_{eq,i}$ , i.e., a vector of internal coordinates ( $\mathbf{R}$ ) referred to a specific origin, then the normal coordinates about one equilibrium geometry can be related to those about any other *via* the configurational coordinates  $\mathbf{R}$ :

$$\mathbf{Q}_2 = \mathbf{L}_2^{-1}(\mathbf{R} - \mathbf{R}_{eq,2}) \quad (3.2)$$

$$= \mathbf{L}_2^{-1}(\mathbf{R} - \mathbf{R}_{eq,1} + \mathbf{R}_{eq,1} - \mathbf{R}_{eq,2}) \quad (3.3)$$

$$= \mathbf{L}_2^{-1}\mathbf{L}_1\mathbf{Q}_1 + \mathbf{L}_2^{-1}(\mathbf{R}_{eq,1} - \mathbf{R}_{eq,2}) \quad (3.4)$$

$$\equiv \mathbf{J}\mathbf{Q}_1 + \mathbf{K}. \quad (3.5)$$



That is, the relationship connecting the two sets of normal coordinates consists of a Duschinsky rotation matrix ( $\mathbf{J}$ ) and a displacement vector ( $\mathbf{K}$ ).

Sharp and Rosenstock use a vectorized extension of the Hermite-function (harmonic oscillator wavefunction) generating function, after taking into account the transformation of variables implied by Eq. 3.5, to express the desired integrals implicitly as coefficients in a power series:

$$\sum_{\mathbf{m}} \sum_{\mathbf{n}} \mathbf{T}^{\mathbf{m}} \mathbf{U}^{\mathbf{n}} (2^{\mathbf{m}} 2^{\mathbf{n}} / \mathbf{m}! \mathbf{n}!)^{1/2} I(\mathbf{m}, \mathbf{n}) = I_0 \exp(\mathbf{T}^{\dagger} \mathbf{A} \mathbf{T} + \mathbf{T}^{\dagger} \mathbf{B} + \mathbf{U}^{\dagger} \mathbf{C} \mathbf{U} + \mathbf{U}^{\dagger} \mathbf{D} + \mathbf{U}^{\dagger} \mathbf{E} \mathbf{T}). \quad (3.6)$$

Here we reproduce the original notation of the paper, which requires some explanation. The normal mode quantum numbers of each of the vibrational states are represented by vectors  $\mathbf{m} = (m_1, m_2, \dots, m_{\mu})$ , while

$$2^{\mathbf{m}} = \prod_i^{\mu} 2^{m_i} \quad (3.7)$$

$$\mathbf{m}! = \prod_i^{\mu} m_i! \quad (3.8)$$

$$\mathbf{T}^{\mathbf{m}} = \prod_i^{\mu} (T_i)^{m_i}. \quad (3.9)$$

$\mathbf{T}$  and  $\mathbf{U}$  (defined analogously to  $\mathbf{U}$ ) are dummy summation vectors, and the other quantities are derived from the Duschinsky transformation as follows:

$$\mathbf{A} = 2\Gamma_2^{1/2} \mathbf{J} \mathbf{Z}^{-1} \mathbf{J}^{\dagger} \Gamma_2^{1/2} - \mathbf{1} \quad (3.10)$$

$$\mathbf{B} = -2\Gamma_2^{1/2} [\mathbf{J} \mathbf{Z}^{-1} \mathbf{J}^{\dagger} \Gamma_2 - \mathbf{1}] \mathbf{K} \quad (3.11)$$

$$\mathbf{C} = 2\Gamma_1^{1/2} \mathbf{Z}^{-1} \Gamma_1^{1/2} - \mathbf{1} \quad (3.12)$$

$$\mathbf{D} = -2\Gamma_1^{1/2} \mathbf{Z}^{-1} \mathbf{J}^{\dagger} \Gamma_2 \mathbf{K} \quad (3.13)$$

$$\mathbf{E} = 4\Gamma_1^{1/2} \mathbf{Z}^{-1} \mathbf{J}^{\dagger} \Gamma_2^{1/2}. \quad (3.14)$$

Here  $\mathbf{Z} = \mathbf{J}^{\dagger} \Gamma_2 \mathbf{J} + \Gamma_1$ , where  $\Gamma_{1,2}$  are diagonal matrices containing the respective scaled normal mode frequencies ( $\omega_i/\hbar$ ), in units of  $\text{amu}^{-1} \text{\AA}^{-2}$ . The normalization

factor is given by

$$I_0 = I(\mathbf{0}, \mathbf{0}) = \left[ \frac{4^\mu \det(\mathbf{\Gamma}_1 \mathbf{\Gamma}_2)}{\det(\mathbf{JZ})^2} \right]^{1/4} \exp[-1/2 \mathbf{K}^\dagger \mathbf{\Gamma}_2 \mathbf{K} + 1/2 \mathbf{K}^\dagger \mathbf{\Gamma}_2 \mathbf{JZ}^{-1} \mathbf{J}^\dagger \mathbf{\Gamma}_2 \mathbf{K}] \quad (3.15)$$

In principle, all desired Franck-Condon overlap integrals can be extracted from the equation above by equating coefficients of like powers of the components of  $\mathbf{T}$  and  $\mathbf{U}$ , although this becomes tedious and eventually impractical for large numbers of modes and/or large values of vibrational quantum numbers. In our case, we only require the overlaps of the lowest few  $T_3$  vibrational levels with a single relatively unexcited vibrational level of  $S_1$ , namely  $3\nu_3$ , and so an algebraic approach is feasible. Thus the following expressions, for example, are easily derived from Eq. 3.15 by collecting terms in the relevant powers of components of  $\mathbf{T}$  and  $\mathbf{U}$ :

$$I(3\nu_3, 0) = (1/48)^{1/2} I_0 (6A_{33}B_3 + B_3^3) \quad (3.16)$$

$$I(3\nu_3, 1\nu_j) = (1/96)^{1/2} I_0 [6A_{33}(B_3D_j + E_{j3}) + B_3^2(B_3D_j + 3E_{j3})], \text{ etc.} \quad (3.17)$$

Such equations provide very useful checks for the results of numerical algorithms.

One straightforward, although computationally costly, method of *numerically* evaluating overlap integrals is by direct differentiation of the Sharp-Rosenstock generating function, since by definition (Eq. 3.6)

$$I(\mathbf{m}, \mathbf{n}) = I_0 (2^{\mathbf{m}} 2^{\mathbf{n}} \mathbf{m}! \mathbf{n}!)^{-1/2} \prod_i \frac{\partial^{m_i}}{\partial T_i^{m_i}} \frac{\partial^{n_i}}{\partial U_i^{n_i}} \exp(\mathbf{T}^\dagger \mathbf{A} \mathbf{T} + \mathbf{T}^\dagger \mathbf{B} + \mathbf{U}^\dagger \mathbf{C} \mathbf{U} + \mathbf{U}^\dagger \mathbf{D} + \mathbf{U}^\dagger \mathbf{E} \mathbf{T}) |_{\mathbf{T}=\mathbf{U}=\mathbf{0}} \quad (3.18)$$

We have implemented a “rough and ready” MATLAB function (`franck.m`) that performs this differentiation symbolically, given  $\mathbf{J}$  and  $\mathbf{K}$ , and vectors of normal mode quantum numbers, as inputs. In order to conserve memory, each component of  $\mathbf{T}$  or  $\mathbf{U}$  is set to zero immediately after its corresponding differentiation is carried out. Running on a laptop, this required only  $\sim 10$  s per overlap integral, which is tolerable, given that we are interested only in a small subset of overlaps for a six-mode system. If the Franck-Condon profile of an entire spectrum is desired, or if the molecule is signif-

icantly larger than acetylene, then a purely numerical approach is advisable. Several authors have described numerical schemes for computing Franck-Condon overlaps, most of which rely upon recursion relations to generate express integrals involving larger values of quantum numbers in terms of those involving smaller ones [40]

### 3.3 Results for Acetylene

The input data for the calculation are the  $\mathbf{L}$  matrices and normal-mode frequencies pertaining to the two minima; these quantities emerge from the standard normal modes analysis, which involves the simultaneous diagonalization of the  $\mathbf{G}$  (internal-coordinate momentum coupling) and  $\mathbf{F}$  (internal-coordinate force constant) matrices:

$$\mathbf{L}^\dagger \mathbf{G}^{-1} \mathbf{L} = \mathbf{1} \quad (3.19)$$

$$\mathbf{L}^\dagger \mathbf{F} \mathbf{L} = \mathbf{\Lambda} = \hbar^2 \mathbf{\Gamma}^2 \quad (3.20)$$

The rationale and details of this calculation are a well-known and long-established part of the theory of vibrational spectroscopy and of classical mechanics, and need not be repeated here. A normal modes analysis may be performed using *ab initio*-derived equilibrium structure parameters and force constants; alternatively, these parameters may be obtained from a fit to experimentally observed vibrational energy-level structure. Tobiasson et al. [47] performed a normal modes analysis based on observed frequencies of both *gerade* and *ungerade* vibrational levels in the  $\tilde{A}^1A_u$  state of all three hydrogen-substituted acetylene isotopomers. This reference, it should be noted, contains a now-infamous typographical error (the quoted equilibrium values of the CC and CH bond lengths are interchanged in the first paragraph). In addition, a reassignment of the  $\nu_1$  fundamental level has lowered the accepted value of that frequency by  $\sim 160 \text{ cm}^{-1}$  [33]. Tables 3.1 and 3.2 below summarize their results. The  $\mathbf{G}$  matrix can be computed from the equilibrium geometry parameters using the general formulae collected in Appendix VI of Ref. [54] and in Ref. [14]; together with the fitted  $\mathbf{F}$  matrix, this is all that is required for the calculation.

Table 3.1:  $\tilde{A}$  State Normal Modes and Harmonic Frequencies, as calculated in Ref. [47]

Mode	Description	Frequency (cm <sup>-1</sup> )
$\nu_1 (a_g)$	Symmetric C-H stretch	3004
$\nu_2 (a_g)$	C-C stretch	1420
$\nu_3 (a_g)$	CCH <i>trans</i> bend	1064
$\nu_4 (a_u)$	HCCH torsion	765
$\nu_5 (b_u)$	Antisymmetric C-H stretch	2914
$\nu_6 (b_u)$	CCH <i>cis</i> bend	785

Table 3.2:  $\tilde{A}$  State Harmonic Force Constants, from fit of Ref. [47]

$F_{rr}$	4.78 mdyne $\text{\AA}^{-1}$	$F_{RR}$	7.63 mdyne $\text{\AA}^{-1}$
$F_{rr'}$	0.138 mdyne $\text{\AA}^{-1}$	$F_{R\theta}$	0.583 mdyne rad <sup>-1</sup>
$F_{rR}$	(0.0)	$F_{\theta\theta}$	0.541 mdyne $\text{\AA} \text{ rad}^{-2}$
$F_{r\theta}$	0.188 mdyne rad <sup>-1</sup>	$F_{\theta\theta'}$	0.127 mdyne $\text{\AA} \text{ rad}^{-2}$
$F_{r'\theta}$	(0.0)	$F_{\tau\tau}$	0.137 mdyne $\text{\AA} \text{ rad}^{-2}$

Table 3.3: Equilibrium Structures of the  $\tilde{A}^1A_u$  State, as quoted in Ref. [47], and of the  $T_3^3B$  State, as calculated in Ref. [50], and in this work

Parameter	$\tilde{A}^1A_u$	$T_3^3B$	
		Ref. [50]	This calculation
$r_{\text{CH}}$	1.097 $\text{\AA}$	1.079 $\text{\AA}$	1.063 $\text{\AA}$
$R_{\text{CC}}$	1.375 $\text{\AA}$	1.352 $\text{\AA}$	1.384 $\text{\AA}$
$\theta_{\text{CCH}}$	122.48°	138.7°	141.6°
$\tau_{\text{HCCH}}$	180.0°	106.1°	107.4°

As can be seen from Table 3.3, the most drastic changes in geometry between the  $\tilde{A}^1 A_u$  and the calculated  $T_3$  structure are the large torsional displacement out of planarity, with accompanying reduction in symmetry, and a significant opening of the CCH bend angles as well. Accordingly, these coordinates are expected to generate the dominant “Franck-Condon active modes” governing trends in overlap between the  $T_3$  vibrational levels and  $S_1 3\nu_3$ .

To complete the calculation, we require computed harmonic force constants around the  $T_3$  minimum, which unfortunately were not reported in the work of Ventura et al [50]. Moreover, due to the reduction in symmetry and the fact the torsion is now a fully symmetric mode and no longer the unique member of its own symmetry species, the required number of force constants increases. Perhaps a useful first approximation would be simply to use the  $S_1$  force constants, anticipating that the qualitative trends in the result will be driven most strongly by the displacement in equilibrium geometries, which is often the case with diatomic molecules [42]. However, this would almost certainly overestimate the overlap integrals, since the  $T_3$  harmonic potential would be modeled by a merely shifted identical copy of the  $S_1$  potential. It is also not certain that such an arbitrary choice would even be consistent with an all-real set of normal-mode frequencies. In order to more quantitatively address the problem, we decided to repeat the *ab initio* calculation of Ref. [50], with a view to determining harmonic force constants about the minimum. Bryan Wong, a graduate student in this research group, performed a time-dependent density functional theory calculation constrained at  $B$  symmetry in  $C_2$  and using Dunning’s correlation consistent basis, cc-pvtz, using the Gaussian 03 package. Harmonic frequencies were obtained numerically by finite differences of numerical gradients. As can be seen from Table 3.3, this calculation was successful in locating a minimum on the  $T_3$  surface with equilibrium structural parameters very similar to those found in Ref. [50]. The normal mode frequencies obtained in this calculation are listed in Table 3.4 below.

Although the traditional Wilson  $\mathbf{F}$ -matrix, with its force constants corresponding to motions directed along valence coordinates, maintains close contact with chemical intuition (ball-and-spring models of nuclear motion), it is not a quantity which

theorists compute directly in *ab initio* vibrational analyses. Instead, a  $3N \times 3N$  “Hessian” matrix containing second derivatives of energy with respect to Cartesian nuclear coordinates, is outputted. This matrix, once transformed to nuclear mass-weighted Cartesian coordinates, can be diagonalized to yield the normal-mode frequencies, of which six (for a nonlinear polyatomic) will be near zero or small; these correspond to the three translational and three rotational coordinates.

If the mass-weighted Hessian is transformed into a basis out of which these motions have been projected, then the eigenvectors will correspond to normal-mode coordinates which neither translate the center of mass nor generate rotational angular momentum to lowest order (Eckart condition) [19]. The  $3N \times (3N - 6)$   $l$ -matrix contains these eigenvectors, which describe each normal coordinate in terms of mass-weighted Cartesian nuclear displacements:

$$l_{\alpha i, k} = \frac{\partial m_i^{1/2} \Delta \alpha_i}{\partial Q_k}, \quad (3.21)$$

in which  $\alpha$  runs over  $x, y, z$ ,  $i$  over the nuclei, and  $k$  over the normal coordinates.

Finally, to make contact with the Sharp-Rosenstock formalism, we use the fact that the  $\mathbf{L}$ -matrix can be calculated from the following:

$$\mathbf{L} = \mathbf{B}\mathbf{M}^{-1/2}\mathbf{1}, \quad (3.22)$$

where  $\mathbf{B}$  is a  $(3N - 6) \times 3N$  matrix, dependent entirely on the equilibrium geometry, relating the internal stretch and bend displacements ( $S_i$ ) to nuclear Cartesian displacements:

$$B_{i, \alpha k} = \frac{\partial S_i}{\partial \Delta \alpha_k}. \quad (3.23)$$

The  $\mathbf{L}$ -matrix contains all the information needed to assess the relative contributions of each internal-coordinate motion to each of the normal modes coordinates. However, this information is conveyed slightly more clearly and intuitively by the *orthogonal* matrix  $\mathbf{T}$  defined as follows:

$$\mathbf{T} = \mathbf{G}^{-1/2}\mathbf{L} \quad (3.24)$$

Table 3.4: Calculated  $T_3$   $^3B$  State Normal Modes and Harmonic Frequencies

Mode	Description	Frequency ( $\text{cm}^{-1}$ )
$\nu_1 (a)$	Symmetric C-H stretch	3630
$\nu_2 (a)$	C-C stretch	2763
$\nu_3 (a)$	HCCH torsion/CCH <i>trans</i> bend	1475
$\nu_4 (a)$	CCH <i>trans</i> bend/HCCH torsion	808
$\nu_5 (b)$	Antisymmetric C-H stretch	3429
$\nu_6 (b)$	CCH <i>cis</i> bend	856

The orthogonality of  $\mathbf{T}$  follows directly from Eq. 3.19:

$$\mathbf{T}^\dagger = \mathbf{L}^\dagger \mathbf{G}^{-1/2} = \mathbf{L}^{-1} \mathbf{G} \mathbf{G}^{-1/2} = \mathbf{L}^{-1} \mathbf{G}^{1/2} = \mathbf{T}^{-1} \quad (3.25)$$

This transformation maps the diagonalization of the generally non-symmetric matrix  $\mathbf{GF}$

$$\mathbf{L}^{-1} \mathbf{G} \mathbf{F} \mathbf{L} = \mathbf{\Lambda} \quad (3.26)$$

(or of  $\mathbf{FG}$ ) onto the orthogonal diagonalization of a symmetric matrix:

$$(\mathbf{G}^{-1/2} \mathbf{L})^\dagger (\mathbf{G}^{1/2} \mathbf{F} \mathbf{G}^{1/2}) (\mathbf{G}^{-1/2} \mathbf{L}) = \mathbf{\Lambda}. \quad (3.27)$$

The  $\mathbf{T}$  matrix of the  $T_3$  normal modes analysis is presented in Table 3.5 below, while in Table 3.4 are displayed the symmetries, dominant characters, and frequencies of the  $T_3$  normal modes, as determined in our *ab initio* calculation. We note in particular that the two symmetric bending modes ( $\nu_3$  and  $\nu_4$ ), involve fairly strong mixing of symmetric CCH bending and the torsion (HCCH dihedral angle), both which are fully symmetric in  $C_2$ . Of the two, the higher-frequency mode ( $\nu_3$ ) contains the greater relative proportion of the torsional vibration, as judged from the relevant  $\mathbf{T}$ -matrix elements.

Any candidate for the doorway state must not only possess the correct vibrational overlap with  $3\nu_3$ , but must also be predicted to fall close enough (within a few  $100 \text{ cm}^{-1}$ ) in energy to result in the observed spectroscopic perturbation (near degeneracy). The calculation of Ref. [50] found the computed  $T_3$  minimum at an

Table 3.5: **T** Matrix for  $T_3$   $^3B$  state, as determined from *ab initio* calculation

	$\nu_1$	$\nu_2$	$\nu_3$	$\nu_4$	$\nu_5$	$\nu_6$
$r_1$	0.4569	0.4411	0.1319	-0.2753	0.6577	-0.2676
$r_2$	0.4569	0.4411	0.1319	-0.2753	-0.6577	0.2676
$R$	-0.6916	0.6920	-0.1398	-0.0797	0.0000	0.0000
$\theta_1$	0.2019	0.2172	-0.3000	0.5111	0.2486	0.6289
$\theta_2$	0.2019	0.2172	-0.3000	0.5111	-0.2486	-0.6289
$\tau$	-0.0265	0.1816	0.6968	0.5571	0.0000	0.0000

Table 3.6: Estimated Energies, and Vibrational Overlaps and Effective Spin-Orbit Matrix Elements with  $S_1$   $3\nu_3$ , of the Lowest-Lying  $T_3$  Vibrational Levels

Level	Energy ( $\text{cm}^{-1}$ )	Overlap	$H_{SO}$ ( $\text{cm}^{-1}$ )
Origin	44,046	-0.0039	-0.053
$1\nu_3$	45,521	0.0083	0.11
$1\nu_4$	44,854	0.0049	0.067
$1\nu_3 + 1\nu_4$	46,329	0.032	0.44
$2\nu_3$	46,996	-0.0111	-0.15
$2\nu_4$	45,662	-0.0021	-0.029

energy of  $5.26 \text{ eV} = 43,230 \text{ cm}^{-1}$  above the ground-state ( $S_0$ ) minimum. Since energy differences between minima are not directly observable, this must be corrected by adding the zero-point energy, i.e., one-half the sum of normal-mode frequencies, to each minimum. Using our calculated  $T_3$  frequencies from above, and the acetylene  $S_0$  frequencies from [46], we find that the  $T_3$  vibrationless level is predicted to lie  $43,230 + (6480-5664) = 44,046 \text{ cm}^{-1}$  above that of the ground state. This, in turn, falls some  $1254 \text{ cm}^{-1}$  below  $S_1$   $3\nu_3$  ( $45,300 \text{ cm}^{-1}$ ). This is a vibrational energy gap that could be bridged by a small (probably 2 or fewer) number of quanta of one or more bending modes. In Table 3.6 we list the predicted vibrational overlap, the resulting effective  $T_3$   $S_1$  spin-orbit matrix element, and the harmonic zeroth-order energy for some of the lowest-lying  $T_3$  vibrational levels.

### 3.4 Rotational Constant Considerations

In addition to the now well-characterized interaction of the  $T_3$  doorway state with low- $J$  values of  $S_1$   $3\nu_3$  ( $K = 1$ ), probably the strongest isolated singlet-triplet interaction



in acetylene observed to date is a very broad Zeeman anticrossing in fluorescence from the rotationless ( $J = K = 0$ ) level of the same state ( $3\nu_3$ ) [21], [18]. From the ZAC spectrum found on page 139 of [21], the position of this anticrossing seen to be 7.14 T, with a width of 0.66 T. The corresponding energy shift is calculated from the magnetic field strength using the relation [21]

$$\Delta E = M_S g \mu_B \Delta B, \quad (3.28)$$

where  $M_S$  is the electronic spin space-fixed projection quantum number ( $\pm 1$  for a pure triplet, assuming the limit of Paschen-Back decoupling),  $g$  is the effective  $g$ -factor (assumed to equal the approximate “bare-electron” value of 2), and  $\mu_B = 9.274 \times 10^{-24}$  J T<sup>-1</sup> is the Bohr magneton. Thus we find for this anticrossing  $\Delta E = 6.67$  cm<sup>-1</sup>. The energy of  $3\nu_3$   $J = K = 0$  is 45,285.7 cm<sup>-1</sup>, placing the zeroth order energy of this triplet perturber at either 45,279.0 or 45,292.4 cm<sup>-1</sup>. From the  $\Delta J = 0$  selection rule, the triplet must also have  $J = 0$  and therefore  $N = 1$ , restricting  $K$  to the values 0 and 1. Information about the strength of the singlet-triplet interaction is provided by the width of the anticrossing; in the classic analysis of Wieder and Eck [53], it is shown that an isolated anticrossing in the “strong coupling” limit (singlet-triplet coupling element much larger than mean depopulation rates) has a Lorentzian lineshape with a full width half maximum (FWHM) given by

$$\frac{1 + \gamma_S/\gamma_T}{(\gamma_S/\gamma_T)^{1/2}} \frac{2V_{ST}}{M_S g \mu_B}, \quad (3.29)$$

where  $\gamma_{S,T}$  are the total (radiative and collisional) depopulation rates of the singlet and triplet state, respectively; under the simplifying approximation  $\gamma_S \approx \gamma_T$ , the prefactor reduces to 2, and the singlet-triplet coupling element is given by one fourth the anticrossing width, converted to units of energy. Thus the measured width of 0.66 T gives an interaction strength of 0.17 cm<sup>-1</sup>. This is strikingly similar in magnitude to the coupling matrix element between  $S_1$   $3\nu_3$  the  $K = 1$  component of the  $T_3$  perturber, extracted from the UV-LIF spectrum. The smaller value of the zeroth order energy falls approximately 21 cm<sup>-1</sup> below the energy of  $S_1$   $3\nu_3$ ; thus we could plausibly

assign the anticrossing triplet perturber as the  $K = 0$  component of the same  $T_3$  vibrational level that appears in our UV-LIF spectrum, provided we can show this to be a reasonable  $K = 0$ ,  $K = 1$  energy separation for  $T_3$ .

An important consideration for judging the likelihood of additional  $T_3 \sim S_1$  near degeneracies is the magnitude of the  $A$  rotational constant, which governs the coarse rotational spacings between sub-bands associated with differing values of  $K$ , the magnitude of the projection of rotational angular momentum along the  $a$ - (least moment of inertia) axis. A straightforward calculation determines  $A_e$  (the value of  $A$  corresponding to the computed equilibrium geometry) as  $24.7 \text{ cm}^{-1}$ , considerably larger than the value observed for vibrational levels of  $S_1$  (typically  $\sim 14\text{-}15 \text{ cm}^{-1}$ ). As is the case for  $S_1$ , the  $a$ -inertial axis is tilted away from the C-C bond axis by a slight angle ( $\sim 6^\circ$ ). The increase in  $A$  is explained largely by the significantly wider CCH bond angle at the  $T_3$  minimum, which brings the structure closer to linearity and consequently reduces the  $a$ -axis moment of inertia. It would be helpful to have a grasp of the dependence of this quantity on the  $T_3$  vibrational quantum numbers, in order to gauge the rotational spacings of  $T_3$  excited vibrational levels. In particular, we expect that  $A$  will be altered in a complicated manner by excitation of the symmetric CCH bending and torsional modes.

A rigorous calculation of vibrationally averaged rotational constants ( $A_v$ ) would involve integration over nuclear coordinate space using exact or approximate vibrational wavefunctions. However, a perturbative treatment exists, by which one can calculate the vibration-rotation interaction constants (denoted  $\alpha$ ) through which the vibrational dependence of  $A$  can be represented by the power series

$$A_v = A_e - \sum_r \alpha_r^A (v_r + 1/2) + \dots \quad (3.30)$$

The result for  $\alpha_r^A$  in the harmonic limit is [34]

$$-\alpha_r^A = \frac{2A^2}{\omega_r} \left[ \sum_\xi \frac{3(a_r^{\alpha\xi})^2}{4I_\xi} + \sum_s (\zeta_{r,s})^2 \frac{(3\omega_r^2 + \omega_s^2)}{\omega_r^2 - \omega_s^2} \right], \quad (3.31)$$

where

$$a_r^{\alpha\beta} = \left( \frac{\partial I_{\alpha\beta}}{\partial Q_r} \right)_e \quad (3.32)$$

and the constants denoted  $\zeta_{r,s}^{(\alpha)}$  are the Coriolis coefficients that define the components of vibrational angular momentum in terms of the normal coordinates and their conjugate momenta:

$$\pi^\alpha = \sum_{r,s} \zeta_{r,s}^\alpha Q_r P_s; \quad (3.33)$$

they are calculable directly from the l-matrix components as follows:

$$\zeta_{r,s}^\alpha = \sum_{\beta\gamma i} \epsilon_{\alpha\beta\gamma} l_{\beta i, r} l_{\gamma i, s}. \quad (3.34)$$

In Equation 3.31 above, the first term represents contributions in first-order perturbation theory from the quadratic dependence of the  $\mu$ -tensor, and therefore also of the rotational constant operator, on the normal coordinates. The second represents the second-order contributions of Coriolis interactions diagonal in  $J$ , but which exchange two quanta of nonidentical normal modes. Both classes of terms contribute to the energy a term in  $(v + 1/2)J(J + 1)$ , and therefore, a term to the rotational constant linear in  $(v + 1/2)$ .

Carrying out the calculation using the parameters derived from the normal mode analysis for  $T_3$  acetylene, we find

$$\alpha_3 = -2.51 \quad (3.35)$$

$$\alpha_4 = 4.82. \quad (3.36)$$

Interestingly, in both cases, the Coriolis contributions dominate the inertial tensor derivative contributions; in the case of  $\nu_4$ , the latter are not sufficient to outweigh the positive contributions of the former (arising from the signs of the resonance denominators), and a *positive*  $\alpha$  results. At any rate, we would expect that one quantum of  $\nu_3$  would lower the value of  $A$  by approximately  $3.8 \text{ cm}^{-1}$ , resulting in a  $K = 0$ ,

Table 3.7:  $a$ -axis Coriolis coefficients for  $T_3$ , calculated from *ab initio* normal-modes analysis

	$\nu_1$	$\nu_2$	$\nu_3$	$\nu_4$	$\nu_5$	$\nu_6$
$\nu_1$	0					
$\nu_2$	0	0				
$\nu_3$	0	0	0			
$\nu_4$	0	0	0	0		
$\nu_5$	-0.038	0.093	0.50	0.30	0	
$\nu_6$	-0.0732	0.092	0.73	0.31	0	0

$K = 1$  separation of approximately  $21 \text{ cm}^{-1}$ , about what is required to account for the ZAC observation.

### 3.5 Assessing the Model and Conclusions

We can tentatively assign the  $T_3$  doorway state to the  $K = 1$  component of a vibrational level containing one quantum of the predominantly torsional/symmetric bending mode  $\nu_3$ , as this state has both the approximately correct predicted energy and interaction matrix element to interact with  $S_1 3\nu_3$ . Furthermore, it also appears that the  $K = 0$  component of this state has previously been observed in Zeeman anticrossing measurements exciting  $S_1 3\nu_3$ ,  $K = 0$ .

The uncertainty in the estimated vibronic energies comprises several contributions: first, of course, the uncertainty of the *ab initio* electronic energy itself; but also that arising from errors in the computed harmonic frequencies, as well as the from the neglect of anharmonicity, which will generally lower the zeroth-order vibrational energies. It would be desirable to perform the same calculation for the energy and frequencies of the  $S_1$  minimum so as to allow computational errors to maximally cancel. This would be particularly crucial for attempting quantitative comparison of  $T_3$  vibrational energies with  $S_1 3\nu_3$ ; in this case, we could hope, the bulk of the error in calculated electronic energies would be filtered out of estimates of energy gaps. Unfortunately, all calculations performed at the same level of theory for  $S_1$  failed to converge. We currently plan on attempting an array of other high-level calculations in order to resolve these issues.

## 3.6 Acknowledgements

We acknowledge the assistance of Bryan Wong in performing electronic structure calculations, and thank Serhan Altunata for helpful suggestions relating to programming.



# Chapter 4

## Statistical Properties of SEELEM Spectra

### 4.1 Introduction and Statement of Problem

In Chapter 2 we have described the detection, via surface electron ejection by laser excited metastables (SEELEM) spectroscopy, of large numbers of predominantly dark, triplet-character eigenstates. A remarkable and rather surprising feature of these observations is the spectral regularity of these states: in spite of the presence of strong and pervasive interactions among the highly vibrationally excited dark states themselves, and the doorway-mediated spin-orbit interaction with the singlet bright state, these states can be arranged into series that fall onto well-behaved rotational term value and Boltzmann intensity plots, in a manner reminiscent of isolated vibrational levels at low vibrational energy. This opens the questions: under what circumstances can strong coupling be expected to result in such apparent regularization of the spectrum? What has one identified when picking out such a “vibrational series” from the observed pattern of spectral lines? In this chapter we describe numerical modeling of doorway-mediated spin-orbit Hamiltonians using random matrices in order to answer these questions.

## 4.2 Random Matrix Theory and Statistical Properties of Spectra

Very highly excited vibrational levels of electronic states are expected to exhibit characteristics of the “chaotic” or “strongly coupled” limit, in which anharmonic and Coriolis interactions have effectively destroyed all normal mode quantum numbers that correspond to classical constants of the motion. In such a situation the observed eigenstate spectrum results from the diagonalization of a Hamiltonian (which would be very difficult to write down in terms of physically as opposed to statistically defined coupling terms) in which each basis state interacts “democratically” and essentially identically with every other state. The spectrum will then be exceedingly difficult to predict with respect to its local, fine details, although it can be characterized by gross statistical metrics (e.g. nearest-neighbor level spacing, longer-range spacing correlations) which are found to be insensitive to the precise values of Hamiltonian matrix elements or to the details of the interactions. The Hamiltonian can consequently be considered to have been drawn at random from an ensemble of Hamiltonians, the matrix elements of which are assumed to be distributed according to some law, and which are constrained to obey relevant symmetry properties. This is the principal result of random matrix theory [31], [38], [44] originally developed to rationalize the complex spectra of quasi-bound excited nuclear states, before the nature of interactions among nucleons was at all understood. Systems of integral total spin and that are invariant under time reversal are described by random matrices drawn from the so-called Gaussian orthogonal ensemble (GOE) of real, symmetric matrices with independently and normally distributed elements. Random matrix theory has rigorously derived nearest-neighbor level spacing statistics for the GOE, which are found to be well approximated by the so-called Wigner surmise:

$$P_W(s) = \frac{\pi}{2} s \exp\left(-\frac{\pi}{4} s^2\right), \quad (4.1)$$



where  $P(s)$  is the probability density associated with a normalized adjacent-level spacing (i.e., spacing divided by average spacing) equal to  $s$ . Notable here is the presence of the prefactor  $s$ , which ensures that  $\lim_{s \rightarrow 0} P(s) = 0$ , i.e., the off-diagonal interactions result in *level repulsion* that reduces the probability of the smallest spacings. By contrast, the exponential spacing distribution function describing “integrable” or non-chaotic systems characterized by Poisson-distributed energy levels, attains its maximum at  $s = 0$ . Two other widely used measures are developed from the “staircase” or integrated density of states function  $n(E, L) = \int_{E-L/2}^{E+L/2} \rho(E) dE$ : the  $\Sigma^2$ , or staircase-function variance statistic, and the  $\Delta_3$  statistic of Dyson and Mehta:

$$\Delta_3(L) = \langle \min_{a,b} \int_{E-L/2}^{E+L/2} [n(E) - a - bE]^2 dE \rangle \quad (4.2)$$

This statistic measures the local (within  $L$  energy units of  $E$ ) mean-square deviation of the integrated state density or “spectral staircase” function from the best-fit linear function that would describe a uniformly spaced spectrum. The brackets represent ensemble averaging, which removes dependence on  $E$ . For the uncorrelated levels of an integrable system, this statistic is linear in  $L$ ; in the case of the GOE, it goes over to logarithmic behavior at large  $L$ , a reflection of the long-range correlation (hence “spectral rigidity”) imposed on the spectrum by the mutual level repulsion.

Typically, a system whose distribution of energy level spacings agrees closely with Eq. 4.1 is said to exhibit quantum chaos. In this regime, adding off-diagonal matrix elements, or altering their magnitude within a certain reasonable range, will alter the eigenvalues, but not their spacing distribution; the chaotic dynamics are therefore said to be robust.

The ideas of random matrix theory have been applied for some time to highly excited molecular spectra. The usual approach is to identify a so-called *pure sequence* of levels characterized by identical values of any remaining good quantum numbers (e.g., total angular momentum, parity) so as to confine the analysis to an unpartitioned subspace of the Hilbert space within which the couplings may be regarded as wholly random. The various statistical measures can then be computed for each pure

sequence and compared to the relevant random matrix theory results.

Although the GOE appears to be a universal limit for strongly interacting systems, numerous authors have discussed the difficulties involved in its application to molecular spectra. The essential difficulty stems from the fact that in the GOE, the magnitudes of off-diagonal elements span the entire energy range of the Hamiltonian matrix. Such a situation is inconsistent with the nature of commonly used molecular basis sets (e.g. harmonic normal-mode oscillators), and results in the wide distribution of individual basis-state characters over the entire spectrum of eigenvalues. By contrast, in molecular spectra (especially in the important cases of intersystem crossing and intramolecular vibrational redistribution), the pattern of the spectrum is imparted by a one or a small number of “feature” or “bright” basis states which are fractionated into a bath of “dark” states over a generally modest energy range. It is for this reason that most spectroscopic experiments are able to access only relatively short sequences of molecular states, in contrast with the large ensembles of hundreds of energy levels assembled from nuclear spectra. Coy, Hernandez, and Lehmann [9] examined a model for the coupling of a sparse bright manifold to a dense dark manifold, in which a small number of bright states is coupled in a delocalized fashion to a prediagonalized, Poisson-distributed bath of dark states. They found that the resulting spectrum exhibits GOE behavior at sufficiently short range, but that intermediate behavior sets in at a range which increases with the number of bright states but which is stable with respect to coupling strength. Perry [37], defined what he termed the “Gaussian-Poisson Ensemble,” in which off-diagonal elements are selected from a Gaussian distribution with mean zero and a variance suitable to the problem at hand, while zeroth-order energies are drawn from a Poisson distribution with a density chosen to achieve the desired density of eigenstates; finally, one basis state near the center of the matrix is singled out as the intensity-carrying bright state. Perry found both that such an ensemble was capable of adequately modeling experimental spectra exhibiting IVR, and that it conformed to GOE behavior with respect to both the Wigner spacing distribution and the  $\Delta_3$  statistic, for reasonable values of mean coupling element relative to mean energy spacing. A subsequent investigation

[20] confirmed this finding in the presence of Coriolis interactions among the coupled bath states.

Our SEELEM spectra sample dark triplet states illuminated by their proximity (within a certain range) to an intensity-lending doorway state feature, which in turn is coupled to the bright state by a weak ( $\sim 0.1 \text{ cm}^{-1}$ ) spin-orbit interaction. This results in the detection of very short ( $< 10$ ) sequences of dark states for which no statistical measure can meaningfully be computed. Nevertheless, we have observed in the spectrum one behavior which could result from underlying chaotic dynamics: the apparent spectral regularization of the dark bath states into vibrational series with smooth dependence on rotational quantum number. The tools of random matrix theory can be used to study numerically the behavior of a dense manifold of strongly coupled dark states interacting with a bright state *via* a single doorway state, in order to investigate the robustness of such regularization with respect to various parameters of the problem.

### 4.3 Numerical Simulations of Doorway-Mediated Coupling Cases

As a first approach to the problem, we have performed straightforward numerical simulations of the  $J$ -dependent eigenvalues of the doorway-mediated spin-orbit Hamiltonian matrix. The model used is in fact very similar to that examined by Perry [37]. We draw zeroth-order dark state energies from a Poisson distribution, which is appropriate for the highly excited overtone and combination energies of a many-vibrational mode system with incommensurate frequencies. Dark~dark coupling matrix elements, which simulate the anharmonic and Coriolis interactions among these highly vibrationally excited states, as well as the spin-orbit matrix elements between these states and the doorway state, are drawn from Gaussian distributions of mean zero. The following statistical distributions are relevant to the simulation:

- *Doorway~dark  $H_{SO}$  coupling matrix elements:* These are drawn from a normal

distribution of mean zero and whose variance yields a mean *absolute value* matrix element of  $0.2 \text{ cm}^{-1}$ , the choice made in the SEELEM intensity simulations of Ref. [3].

- *Dark~dark anharmonic and Coriolis coupling matrix elements:* These are again drawn from a normal distribution of mean zero, the standard deviation of which is a control parameter gauging the strength of the dark-dark interactions, ranging from  $0.1$  to  $5 \text{ cm}^{-1}$ .
- *Zeroth-order dark state energies:* These are drawn from a Poissonian distribution, simulating the high-energy level pattern of the integrable system of six decoupled harmonic vibrational modes, parametrized by a mean density of states consistent with the observed dark state density ( $\sim 5/\text{cm}^{-1}$ ).
- *Zeroth-order dark state rotational constants:* These are drawn from a normal distribution whose mean will be treated as a control parameter defining various cases of the problem. The variance should reflect the expected variance in structural properties of the zeroth-order basis states.

In addition, the experimentally observed values for the  $S_1$  bright state and  $T_3$  doorway state energies and rotational constants, and for the  $S_1 \sim T_3$  spin-orbit coupling matrix element, are inputted. The bright and doorway states are placed in the center of a  $200 \times 200$  matrix of dark states (a reasonably large size was chosen to eliminate edge effects). For each set of input parameters, the resulting  $H_{eff}$  matrix is diagonalized for each value of  $J$  and the eigenvalues plotted versus  $J(J+1)$  to yield synthetic “rotational term value plots” such as were presented for experimental data in Chapter 2. The results for various cases are presented in the figures below.

The key problem that confronts us when examining a such a “raw” reduced rotational term value plot, whether it represents experimentally observed or simulated energies, is that of picking out rotational series in an unbiased fashion that is capable of being automated in an algorithmic sense. Intuitively, we might expect that if the energies of a series of eigenstates fall along a well-behaved term value plot, then their

eigenvectors will exhibit similar composition in the zeroth-order basis. A convenient measure of this property is the simple overlap or dot product of eigenvectors with one another. Thus a simple way of proceeding is to pick out, at the lowest value of  $J$ , a number of eigenstates clustered in energy around the dominantly bright and doorway states. Then, we associate with each of these eigenstates the eigenstate at the next value of  $J$  with which it has the largest absolute value of overlap. This process is continued with each successive  $J$ -value, so that a number of vibrational series can be built up and its reduced term value plot examined for regularity. Some representative samples are displayed in Figs. 4-1 through 4-4, for the case where  $\langle B_{\text{dark}} \rangle = B_{\text{doorway}} = 1.142\text{cm}^{-1}$ , and for four different variances of the dark-dark coupling element distribution. Specifically, the root-mean-square coupling element (which is equal to the standard deviation) is increased from 0.1 to 0.5, 1, and 5  $\text{cm}^{-1}$ , respectively, corresponding to coupling parameters (density of states times rms coupling element) of 0.5, 2.5, 5, and 25, respectively. It is seen that as the magnitude of dark-dark coupling is increased, the maximum-overlap criterion is picking out series of eigenstates that fall on term value plots of increasing smoothness and linearity.

## 4.4 Remarks and Conclusions

We have found strong evidence for the association of the observed regularization of rotational term energy plots with strong coupling among the coupled dark states. This finding, along with the observation of a dark state density comparable to the total density of states expected from direct-count estimates (see Chapter 2), supports the conclusion that the  $T_{1,2}$  vibrational states observed *via* doorway-mediated spin-orbit coupling in our SEELEM spectra are in the “strongly coupled” or “chaotic” limit. It would, however, be optimal to place this conjecture on a firmer statistical basis by devising some numerical measure of spectral regularity, which could be averaged over many realizations of the random-matrix Hamiltonian. Work in this direction is continuing.

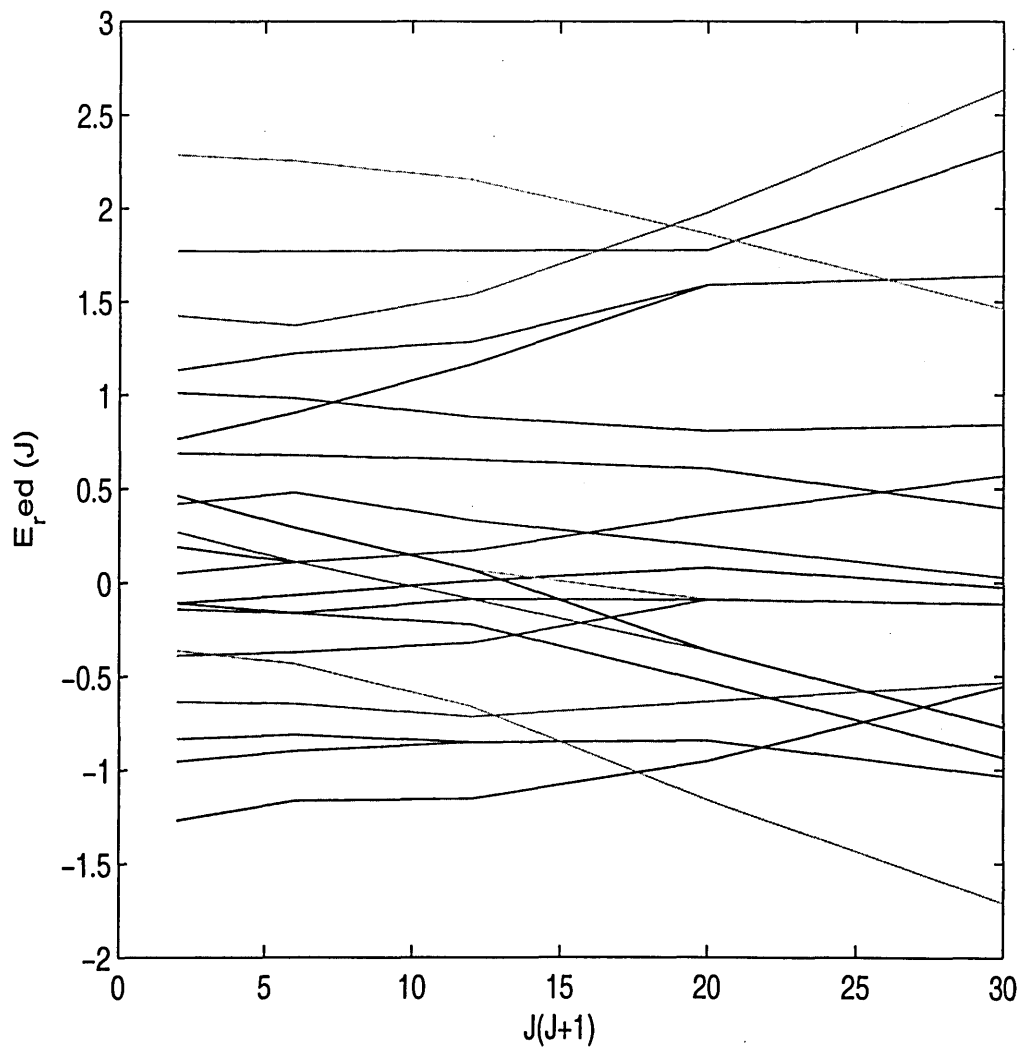


Figure 4-1: A simulated rotational term plot, with  $\langle B_{\text{dark}} \rangle = B_{\text{doorway}}$  and  $\langle H_{\text{dark-dark}}^2 \rangle^{1/2} = 0.1 \text{ cm}^{-1}$ .

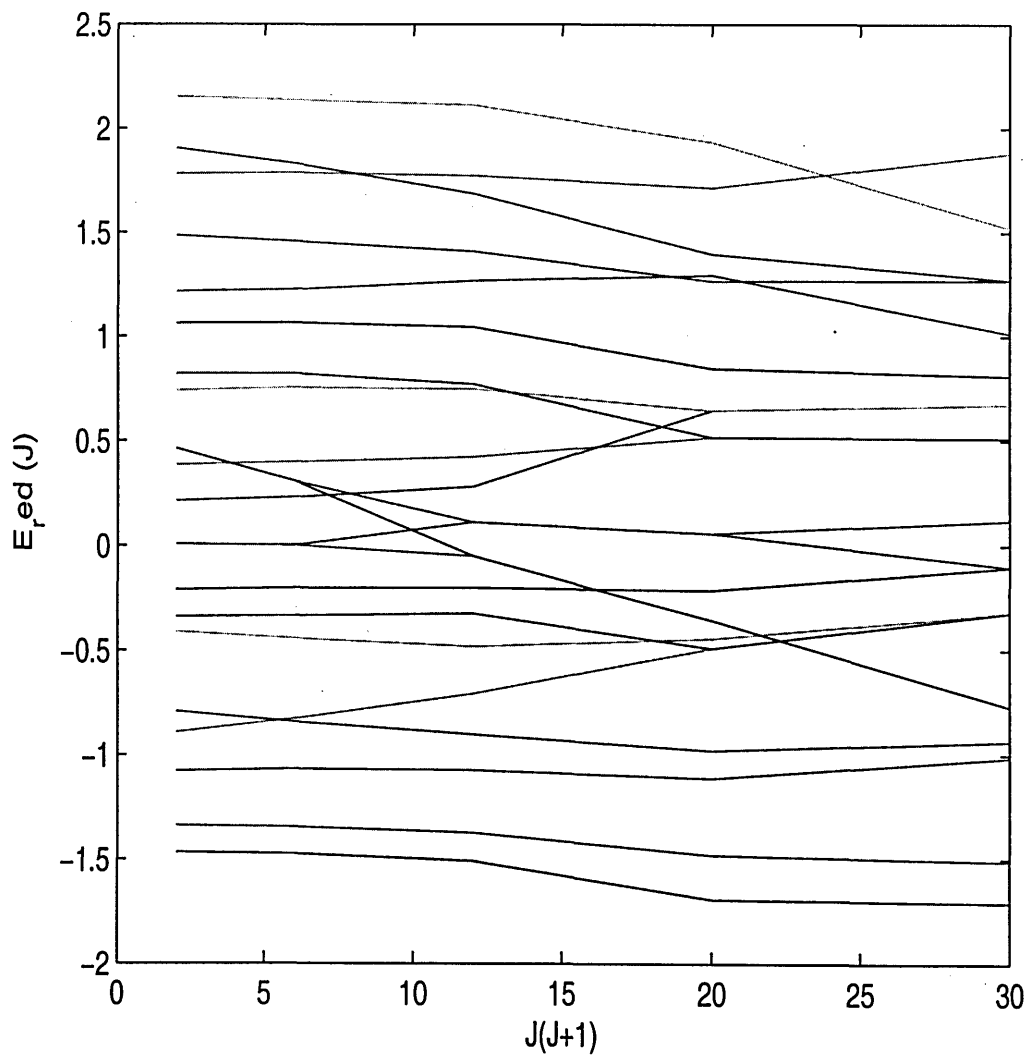


Figure 4-2: Same as previous, but with  $\langle H_{\text{dark-dark}}^2 \rangle^{1/2} = 0.5 \text{ cm}^{-1}$ .

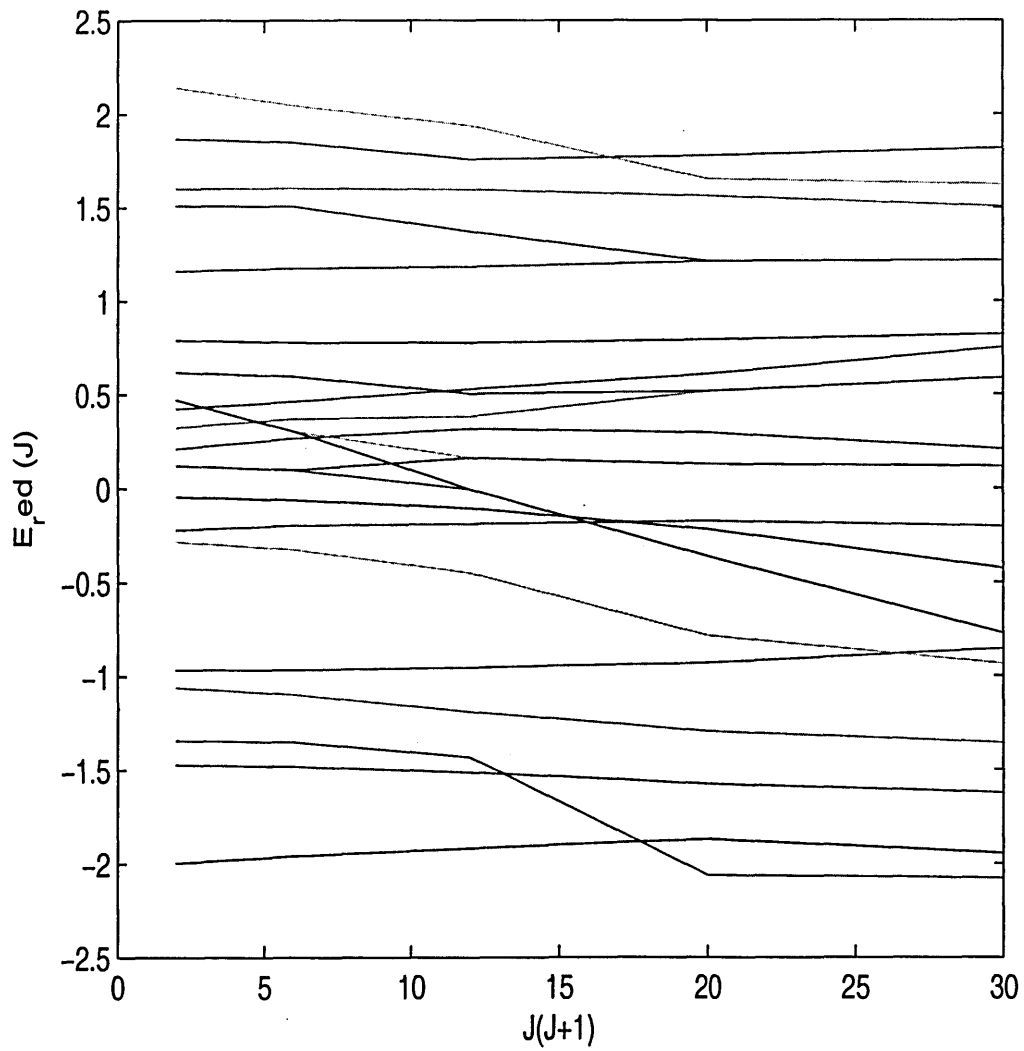


Figure 4-3: Same as previous, but with  $\langle H_{\text{dark-dark}}^2 \rangle^{1/2} = 1 \text{ cm}^{-1}$ .



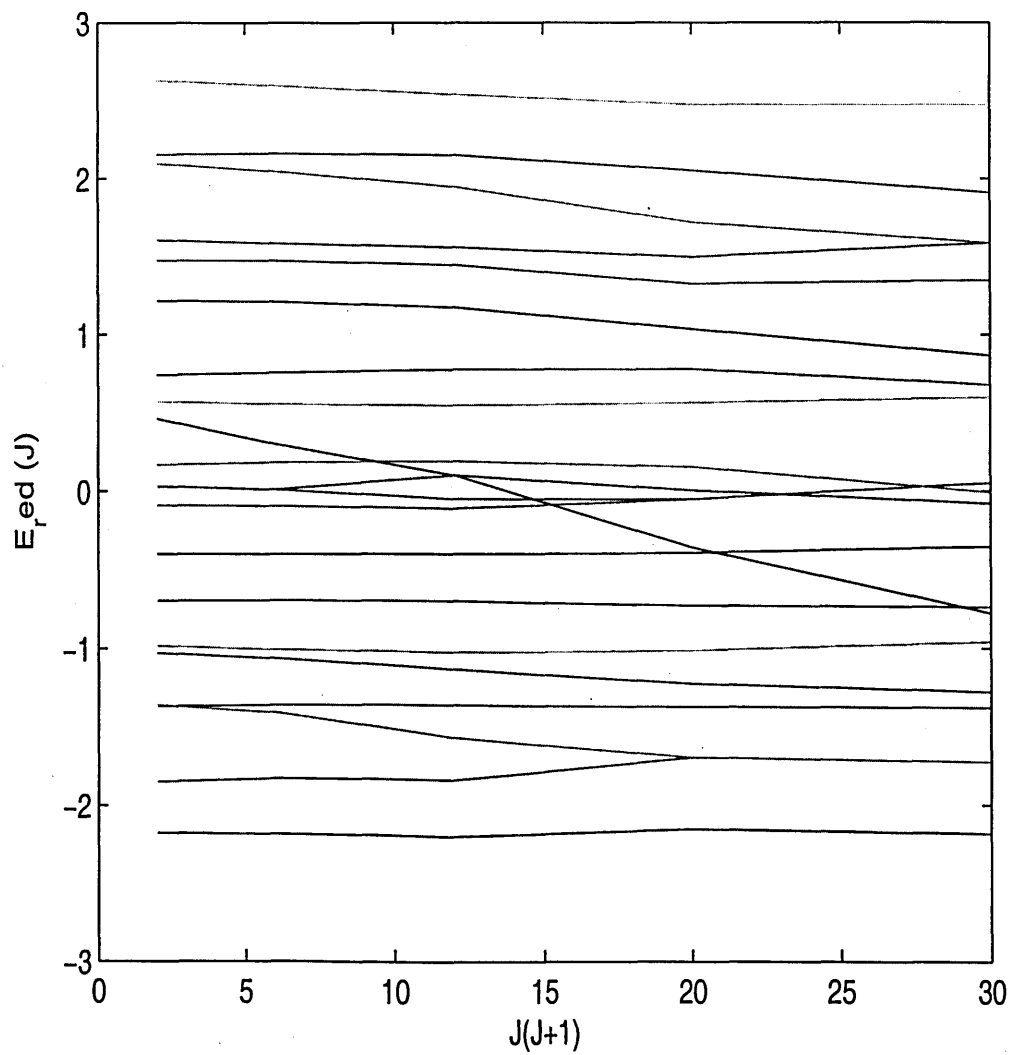


Figure 4-4: Same as previous, but with  $\langle H_{\text{dark-dark}}^2 \rangle^{1/2} = 5 \text{ cm}^{-1}$ .



# Chapter 5

## A High-Resolution SEELEM Spectrometer

### 5.1 Motivation

A major area of present effort on this project is the replacement of our YAG-pumped, frequency doubled nanosecond-pulse dye laser ( $\Delta\tilde{\nu} = 0.03 \text{ cm}^{-1}$ ) with an excitation source of considerably higher spectral resolution. This is desirable for at least two reasons:

- *Sensitivity* is limited by attainable signal-to-noise, which in turn is limited by laser resolution: at constant integrated line intensity, the narrower the linewidth, the higher the peak line intensity. Higher resolution simply allows a larger number of weak features to stand out above the noise. This is critical for observing the very weak singlet-triplet transitions we hope to detect on Au- or Cs-SEELEM.
- *Multiphoton destruction processes* are a ubiquitous hazard when probing weakly allowed molecular transitions at UV excitation wavelengths. This is so because at the two-photon level there will always be found a dense manifold of highly predissociation-broadened Rydberg states of both spin characters. Thus, when attempting to detect a weak singlet-triplet transition by means of SEELEM

(or any other technique sensitive to population remaining in the intermediate level), the broad but vastly more intense triplet valence-triplet Rydberg transition will overwhelm the sharp but weak singlet-triplet transition, and severely limit the attainable population in the intermediate level. Indeed, for the  $V_0^3 K_0^1 \tilde{A}^1 A_u \leftarrow \tilde{X}^1 \Sigma_g^+$  transition in acetylene, the two-photon energy is  $\sim 90,600 \text{ cm}^{-1}$ , only  $1350 \text{ cm}^{-1}$  below the ionization threshold. This energy corresponds to an effective principal quantum number of  $\sim 9$ . Acetylene Rydberg states of much lower  $n^*$  are known to be dissociatively broadened with widths as large as  $5 \text{ cm}^{-1}$  (corresponding to lifetimes on the order of 1 ps). Strong experimental evidence for the presence of these destructive processes is provided by both the observation of early-arriving metastable photofragment signal in the SEELEM time-of-flight (TOF) spectrum [12], and the detection of near-infrared emission that is plausibly assignable to electronically excited acetylene photofragments but not to the parent molecule itself [3].

Thus it is clear that higher resolution, by an order of magnitude or more, is desirable. Any pulsed radiation source of pulse duration  $\tau$  is constrained to have a frequency bandwidth greater than or equal to the Fourier limit,  $\Delta\tilde{\nu} \sim 1/\tau$ . This limit is rarely if ever attained in pulsed dye lasers, for a variety of reasons. Indeed, the Fourier limit corresponding to a 5 ns pulse duration is  $\sim 0.006 \text{ cm}^{-1}$ . A common technique for producing Fourier-limited pulses with energies suitable for harmonic conversion is pulsed dye amplification of single transverse mode, single frequency cw radiation. The fundamental wavelengths required for our experiment (around 440 nm) can be readily produced by single frequency ring lasers operating with blue dyes, or by doubling the infrared output of a titanium:sapphire ring laser. This latter route requires the doubling to be done either inside the laser cavity itself, or in an external stabilized doubling cavity, in order to build up sufficient circulating intensity for efficient conversion. Despite the complexity involved in two frequency doubling steps, we chose the second method, which avoids the inconveniences associated with the operation of ring lasers with blue dyes (low attainable powers, frequent dye changes, narrow spectral coverage), and enjoys the advantages of the Ti:sapphire laser medium:

a broad gain curve, good thermal and mechanical stability and ruggedness.

## 5.2 Design of the Single-Frequency Cw Laser Spectrometer

The core of our spectrometer is the Coherent 899-29 scanning actively stabilized single-frequency titanium:sapphire laser. The Ti:Sapphire medium provides gain over the range 680 - 1100 nm, in conjunction with three sets of mirror optics that allow operation over the ranges 680-850 nm (short wave), 800-930 nm (medium wave), and 900-1100 nm (long wave). A stack of frequency filters (birefringent filter, thin etalon, thick etalon) select a single longitudinal mode, while servo electronics that actively stabilize the cavity to a sealed, thermally stabilized Fabry-Perot cavity to provide a spec rms linewidth of 500 kHz. Continuous frequency tuning with tracking of the filter stack is possible over 20 GHz intervals. The 899-29 version features the Autoscan wavemeter and computer interface, which performs continuous concatenation of these 20 GHz short scans to allow seamless scanning over experimentally convenient ranges.

The output of this laser is coupled into a Spectra-Physics (originally manufactured by LAS) WaveTrain external cavity doubler. This device is built around a passive resonator consisting of two mirrors and a piezo-mounted prism that modulates the effective cavity length. Within the cavity is an lithium borate (LBO) crystal, cut for phase matching at a fundamental wavelength of 887 nm. The second harmonic range of the doubler is limited by the reflectivity of the mirrors to between 420 and 480 nm; additional optics sets for other wavelengths can be ordered. In order to maximize second harmonic conversion, the resonator cavity is locked to the ring laser frequency by means of the Pound-Drever-Hall method [17], in which radio frequency (80 MHz) sidebands are imposed on the spectrum of the incident fundamental by an electro-optic phase modulator. A detector positioned by the entrance mirror of the cavity monitors the superposition of promptly reflected sideband radiation and phase-delayed leakage radiation from the cavity. The amplitude of the component

of this signal oscillating at twice the modulation frequency provides a signed error signal around the resonance configuration of the cavity. Servo amplifiers drive the prism piezo to modulate the cavity length in response to this error signal. (A good pedagogical introduction to the Pound-Drever-Hall method is contained in Ref. [5].) At input fundamental powers of 700-900 mW, doubled output on the order of 50 mW is routinely achievable.

### 5.3 Initial Results

As a test of our high resolution tunable cw visible source, we recorded a portion of the laser induced fluorescence (LIF) excitation spectrum of the  $\text{NO}_2$  molecule near  $23,582 \text{ cm}^{-1}$  in our skimmed molecular beam apparatus (described in Chapter 2). In Fig. 5-1 we display a fine structure doublet ( $N' = 1$ ; the two spin components correspond to  $J' = 0.5$  and  $1.5$ ). This spectrum was obtained with a beam of 1%  $\text{NO}_2$  in He, at a total backing pressure of 625 Torr. The laser was continuously scanned at a rate of  $10 \text{ MHz s}^{-1}$  in the second harmonic, while the output of a PMT was averaged over 30 shots of the 10 Hz pulsed valve, resulting in a resolution element of 30 MHz per data point. Three spectra were collected and averaged together. The lines fit well to Gaussian lineshapes with a full width half maximum (FWHM) of  $0.010 \text{ cm}^{-1}$  or 340 MHz. The resolution is expected to be limited by the transverse Doppler width of the molecular beam, and thus this experiment provides a measure of that quantity. A rough estimate of the Doppler width can be computed using geometrical properties of the apparatus, after making some simple measurements. Thus, by measuring fluorescence at two points of known separation before and after the skimmer, and comparing the fluorescence delay times with respect to the firing of the nozzle, the beam velocity is estimated to be  $1800 \text{ m s}^{-1} = 1.8 \text{ mm } \mu\text{s}^{-1}$ . The 3 mm-diameter skimmer located 6 cm from the nozzle orifice selects a cone of molecules of angular spread  $2 \tan^{-1} \left( \frac{1.5}{60} \right) = 2 \tan^{-1}(0.025)$ . This tangent is the ratio of maximum transverse velocity to longitudinal beam velocity, so the maximum transverse velocity allowed by the skimmer is  $0.025 \times 1800 \text{ m s}^{-1} = 45 \text{ m s}^{-1}$ . Finally,

the transverse velocity spread as a fraction of the speed of light gives the Doppler broadening as a fraction of transition frequency:

$$\Delta\tilde{\nu} \approx \frac{\Delta v_{\text{transverse}}}{c} \tilde{\nu}_{\text{transition}} = \frac{45 \text{ m s}^{-1}}{3 \times 10^8 \text{ m s}^{-1}} 23,583 \text{ cm}^{-1} = 0.007 \text{ cm}^{-1}, \quad (5.1)$$

which is in satisfactory order-of-magnitude agreement with our experimental linewidth; a more stringent test of the cw linewidth would require a subdoppler technique.

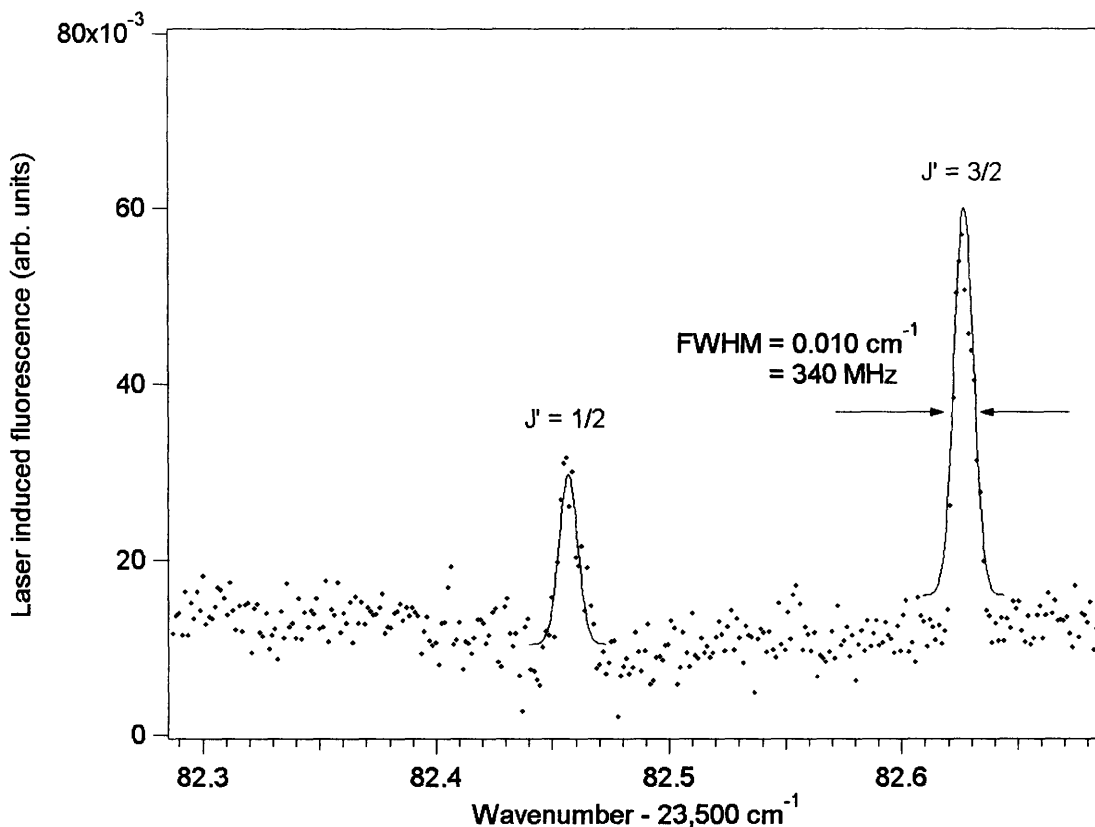


Figure 5-1: NO<sub>2</sub> laser induced fluorescence (LIF) excitation spectrum near 23,582 cm<sup>-1</sup>, showing Doppler-limited linewidth, demonstrating the capabilities of our high resolution visible cw laser. Spectrum was recorded with molecular beam of 1% NO<sub>2</sub> in He, at backing pressure of 625 Torr.

## 5.4 Future Prospects

In order to use this laser system for acetylene SEELEM spectroscopy, the visible cw radiation must be pulse amplified so that it may be single-pass frequency doubled

in BBO. A commonly used method for pulse dye amplification employs the Bethune cell [4], in which the seed radiation passes through a bore in the dye cell that is isotropically pumped by various division of the pump beam resulting from reflections off the prism-like faces of the cell. Several Bethune cells of lengths and bore diameters are available in the laboratory. The optimization of a pulsed dye amplifier chain is something of an art; a number of parameters including dye concentrations, and spatial beam filtering between amplifier stages, must be adjusted to achieve optimal gain and minimal amplified spontaneous emission (ASE). Once this is done, it should be possible to achieve Fourier-limited pulses of sufficient energy and linewidth to record a high-quality, high-resolution SEELEM  $S_1$   $3\nu_3$  spectrum.



# Chapter 6

## Conclusion

The principal achievement of the work described in this thesis has been the thorough characterization of doorway-mediated intersystem crossing in acetylene: we have described in some detail the properties of the bright state, made plausible identifications of the doorway state, and observed interesting dynamical properties of the manifold of coupled dark states. Such an analysis can serve as a paradigm for what is possible in the study of complicated molecular dynamics using a multispectral approach such as our simultaneously recorded UV-LIF/SEELEM technique. However, it would be fair to say that we have come up against severe limitations of this apparatus, particularly of the SEELEM detection scheme. The SEELEM detection channel was a source of great frustration in terms of obtaining and optimizing signal on a daily basis. Some key experimental desiderata are listed below:

- A much more robust SEELEM detector, and one which is easier to maintain and optimize on a daily basis, is required. Despite numerous attempts to improve the detector loading procedure, and in particular to optimize the electron optics which guide the SEELEM electrons to the electron multiplier, no significant enhancement of previous Au-SEELEM signal was observed. It appears that much work remains to be done before the SEELEM detector can be considered a “mature” apparatus.
- The mastery of SEELEM detection using alkali metals must be achieved. While

alkalis like Cs, which must be continuously vapor-deposited onto some substrate, are certainly inconvenient to work with in comparison with stable foils like Au or Ag, their low work functions ( $< 3$  eV) are required to detect the lowest-lying triplet electronic states of acetylene ( $T_{1,2}$ ). Since these are the only acetylene triplet states that have previously been studied in rotationally resolved measurements [52], [26], the detection of  $T_{1,2}$  levels (at low vibrational energies, where their vibrational states have assignable, well-defined character in a normal-mode basis) would be especially exciting. Unfortunately, Cs-SEELEM detection proved to be still more frustrating than Au. The most stringent design problem in this case is finding a convenient means of water-cooling the rotating wheel upon which the Cs is deposited, which is an extremely challenging engineering problem. However, such cooling is vital to minimize the dark electron counts of the Cs surface. Above all, any system must couple both rotational motion and cooling water into the vacuum chamber without any vacuum degradation.

- The use of alternate excitation methods with SEELEM detection needs to be explored. While laser excitation enjoys the great advantage of rotationally resolved detection and state preparation, it is severely limited in relying upon whatever spin-orbit coupling is present to make nominally spin-forbidden transitions weakly allowed. In the case of acetylene (and other hydrocarbons) this coupling is very weak indeed ( $\sim 0.1$  cm<sup>-1</sup>), and it is doubtful whether isolated rotationally resolved singlet-triplet transitions in acetylene will ever be detected with SEELEM using gold or any other metal surface. Some possibilities include electron-impact excitation, and excitation by collisional energy transfer from photosensitized metastable Hg, or some other metastable species. Such a technique could be capable of transferring significant population into low-lying acetylene triplet states from which spin-allowed triplet-triplet transitions could be excited, with the upper states detected on various SEELEM surfaces. Attempts to incorporate metastable Hg excitation into the present apparatus are

underway.

As a more immediate goal, the use of a higher-resolution excitation laser with Au-SEELEM is desirable in order to measure the highly congested  $S_1$   $3\nu_3$  spectrum described above to higher precision and signal-to-noise. This would put the analysis described in Chapter 2 on a more secure footing. A high-resolution visible cw laser spectrometer has been made operational, as described in Chapter 5, in which the broadly tunable (680-1100 nm), single-frequency (500 kHz rms linewidth) infrared output of a cw titanium:sapphire ring laser (Coherent 899-29 with Autoscan) is frequency doubled in an LBO crystal in an actively stabilized resonant cavity (Spectra-Physics WaveTrain). Powers of up to 50 mW in the blue are thereby attained. In order to obtain the UV wavelengths required for acetylene  $S_1$  excitation, this cw radiation must be pulse-amplified (in Nd:YAG third-harmonic pumped dye cells) and the resulting pulsed radiation doubled in a single pass through a BBO crystal. It will be possible to achieve Fourier-limited laser linewidths on the order of  $0.005\text{ cm}^{-1}$  in the UV—an order of magnitude improvement over the present frequency-doubled pulsed dye laser output. Such a capability would make possible a spectacular new view of the spectra reported in this work.



# Bibliography

- [1] E. Abramson, R. W. Field, D. Imre, K. K. Innes, and J. L. Kinsey. *J. Chem. Phys.*, 83:453, 1985.
- [2] M. Ahmed, D. S. Peterka, and A. G. Suits. *J. Chem. Phys.*, 110:4248, 1999.
- [3] Selen Altunata. *Intersystem Crossing in Acetylene: A Mechanistic Study*. PhD thesis, Massachusetts Institute of Technology, 2001.
- [4] D. Bethune. *Appl. Opt.*, 20:1897, 1981.
- [5] E. D. Black. *Am. J. Phys.*, 69(1):79, 2001.
- [6] J. C. D. Brand and C. G. Stevens. *J. Chem. Phys.*, 58(8):3331, 1973.
- [7] Jack Cariou and Paul Luc. *Atlas Du Spectre d’Absorption de la Molecule de Tellur*. Orsay (France), 1980.
- [8] E. U. Condon and G. H. Shortley. *The Theory of Atomic Spectra*. Cambridge University Press, London, 1953.
- [9] S. L. Coy, R. Hernandez, and K. K. Lehmann. *Phys. Rev.*, 40:5935, 1989.
- [10] Q. Cui and K. Morokuma. *Chem. Phys. Lett.*, 272:319, 1997.
- [11] Q. Cui, K. Morokuma, and J. F. Stanton. *Chem. Phys. Lett.*, 263:46, 1996.
- [12] Kevin L. Cunningham. *Surface Electron Ejection by Laser Excited Metastables Spectroscopy of Acetylene*. PhD thesis, Massachusetts Institute of Technology, 2000.

- [13] H. L. Dai, C. L. Korpa, J. L. Kinsey, and R. W. Field. *J. Chem. Phys.*, 82:1688, 1985.
- [14] J. C. Decius. *J. Chem. Phys.*, 16:1025, 1948.
- [15] A. E. Douglas. *J. Chem. Phys.*, 45:1007, 1966.
- [16] M. Drabbels, J. Heinz, and W. L. Meerts. *J. Chem. Phys.*, 100:165, 1994.
- [17] R. W. Drever, J. L. Hall, and F. V. Kowalski. *Appl. Phys. B*, 31:97, 1983.
- [18] P. Dupre, R. Jost, M. Lombardi, P. G. Green, E. Abramson, and R. W. Field. *Chem. Phys.*, 152:293, 1991.
- [19] C. Eckart. *Phys. Rev.*, 47:552, 1935.
- [20] J. Go and D. S. Perry. *J. Chem. Phys.*, 103(13):5194, 1995.
- [21] Peter Gordon Green. *Acetylene Near Dissociation: Novel Effects of External Fields*. PhD thesis, Massachusetts Institute of Technology, 1989.
- [22] J. T. Hougen. *Can. J. Phys.*, 42:433, 1964.
- [23] J. T. Hougen and J. K. G. Watson. *Can. J. Phys.*, 43:298, 1965.
- [24] C. K. Ingold and G. W. King. *J. Chem. Soc.*, page 2702, 1953.
- [25] K. K. Innes. *J. Chem. Phys.*, 22:863, 1954.
- [26] H. Kanamori. private communication.
- [27] W. D. Lawrance and A. E. W. Knight. *J. Chem. Phys.*, 89:917, 1985.
- [28] H. Lischka and A. Karpfen. *Chem. Phys.*, 102:77, 1986.
- [29] M. M. Mizoguchi, N. Yamakita, S. Tsuchiya, A. Iwasaki, K. Hoshina, and K. Yamanouchi. *J. Chem. Phys.*, 104:10212, 2000.
- [30] A. R. W. McKellar, P. R. Bunker, T. J. Sears, K. M. Evenson, R. J. Saykally, and S. R. Langhoff. *J. Chem. Phys.*, 79:5251, 1983.

- [31] M. L. Mehta. *Random Matrices*. Academic Press, San Diego, second edition, 1991.
- [32] A. Merer. private communication.
- [33] A. J. Merer, N. Yamakita, S. Tsuchiya, J. F. Stanton, Z. Duan, and R. W. Field. *Mol. Phys.*, 101(4):663, 2003.
- [34] I. M. Mills. Vibration-rotation structure in asymmetric- and symmetric-top molecules. In *Molecular Spectroscopy: Modern Research*. Academic Press, 1972.
- [35] N. Ochi and S. Tsuchiya. *Chem. Phys. Lett.*, 140:20, 1987.
- [36] N. Ochi and S. Tsuchiya. *Chem. Phys.*, 152:319, 1991.
- [37] D. S. Perry. *J. Chem. Phys.*, 98(9):6665, 1993.
- [38] C. E. Porter. *Statistical Properties of Spectra: Fluctuations*. Academic Press, New York, 1965.
- [39] W. T. Raynes. *J. Chem. Phys.*, 41(10):3020, 1964.
- [40] P. T. Ruhoff and M. A. Ratner. *Int. J. Quant. Chem.*, 77:383, 2000.
- [41] G. J. Scherer, Y. Chen, R. L. Redington, J. L. Kinsey, and R. W. Field. *J. Chem. Phys.*, 85:6315, 1986.
- [42] T. E. Sharp and H. M. Rosenstock. *J. Chem. Phys.*, 41(7):3453, 1964.
- [43] C. G. Stevens and J. C. D. Brand. *J. Chem. Phys.*, 58(8):3324, 1973.
- [44] H.-J. Stöckmann. *Quantum Chaos*. Cambridge University Press, Cambridge, 1999.
- [45] T. Suzuki, Y. Shi, and H. Kohguchi. *J. Chem. Phys.*, 106:5292, 1997.
- [46] M. A. Temsamani and M. Herman. *J. Chem. Phys.*, 102(16):6371.

- [47] J. D. Tobiasson, A. L. Utz, E. L. Sibert, III, and F. F. Crim. *J. Chem. Phys.*, 99:5762, 1993.
- [48] A. L. Utz, J. D. Tobiasson, E. Carrasquillo, L. J. Sanders, and F. F. Crim. *J. Chem. Phys.*, 98:2742, 1993.
- [49] J. H. Van Vleck. *Rev. Mod. Phys.*, 23:213, 1951.
- [50] E. Ventura, M. Dallos, and H. Lischka. *J. Chem. Phys.*, 118(4):1702, 2003.
- [51] J. K. G. Watson, M. Herman, J. C. V. Craen, and R. Colin. *Journal of Molecular Spectroscopy*, 95:101, 1982.
- [52] H. R. Wendt, H. Hippler, and H. E. Hunziker. *J. Chem. Phys.*, 70:4044, 1979.
- [53] H. Wieder and T. G. Eck. *Phys. Rev.*, 153:103, 1967.
- [54] E. B. Wilson, J. C. Decius, and P. C. Cross. *Molecular Vibrations: the theory of infrared and Raman spectra*. McGraw-Hill, 1955.



## Curriculum Vitae

BIRTH DATE: August 14, 1978.

EDUCATION: Marquette University, BS and BA *summa cum laude* (1999); Massachusetts Institute of Technology, Ph.D. expected June 2006.

AWARDS AND HONORS: Lester Wolfe Fellowship, MIT G. H. Harrison Spectroscopy Laboratory (2002); National Science Foundation East Asia Graduate Fellowship (2002); Phi Beta Kappa; Merck Index Award for Scholarship in Chemistry, Marquette University (1999); Distinguished Scholarship (full tuition), Marquette University (1996).

### PUBLICATIONS AND PRESENTATIONS:

B. M. Wong, R. L. Thom, and R. W. Field. "Accurate Inertias for Large-Amplitude Motions: Improvements on Prevailing Approximations." *Journal of Physical Chemistry* (2006).

A. P. Mishra, R. L. Thom, and R. W. Field. "New  $S_1$  state vibrational and  $T_{3,2,1}$  spin-rotational assignments in the vicinity of the acetylene  $\tilde{A}^1A_u - -\tilde{X}^1\Sigma_g^+ V_0^3K_0^1$  band." *Journal of Molecular Spectroscopy*, 228, 565 (2004).

S. Altunata, K. L. Cunningham, M. Canagaratna, R. Thom, and R. W. Field. "The mechanism of surface electron ejection by laser excited metastables." *Journal of Physical Chemistry* 106 (7), 1122 (2002).

Presented research at four meetings of the International Symposium on Molecular Spectroscopy, The Ohio State University, Columbus, OH, and at various symposia in Japan.